ATLAS Paper Draft

Search for supersymmetry at $\sqrt{s} = 13$ TeV in final states with jets and two same-sign leptons or three leptons with the ATLAS detector

SUSY-2015-09

Version: 3.2

To be submitted to: Eur. Phys. J. C

Supporting internal notes

Supporting note: https://cds.cern.ch/record/2052581

Comments are due by: February 25th, 2016

Abstract

A search for strongly produced supersymmetric particles is conducted using signatures involving multiple energetic jets and either two isolated leptons (e or μ) with the same electric charge or at least three isolated leptons. The search also utilises b-tagged jets, missing transverse momentum and other observables to extend its sensitivity. The analysis uses a data sample of proton–proton collisions at $\sqrt{s} = 13$ TeV recorded with the ATLAS detector at the Large Hadron Collider in 2015 corresponding to a total integrated luminosity of 3.2 fb^{-1}. No significant excess over the Standard Model expectation is observed. The results are interpreted in several simplified supersymmetric models and extend the exclusion limits from previous searches. In the context of exclusive production and simplified decay modes, gluino masses are excluded at 95% confidence level up to 1.1–1.3 TeV for light neutralinos (depending on the decay channel), and bottom squark masses are also excluded up to 540 GeV. In the former scenarios, neutralino masses are also excluded up to 550-850 GeV for gluino masses around 1 TeV.

Document created on 26th February 2016 using ATLAS LaTeX Version 01-07-07.

Analysis Team

[*email:* atlas-SUSY-2015-09-editors@cern.ch]

B. Abbott, J.-F. Arguin, S. Berlendis, F. Cardillo, G. Carrillo-Montoya, A. Di Simone, O. Ducu, D. Gerbaudo, F. Hubaut, G. Herten, S. Kahn, A. Lleres, J. Maurer, E. Monnier, T. Nguyen, A. Paramonov, J. Poveda, P. Pralavorio, H. Ren, O. Rifki, Y.-T. Shen, P. Skubic, A. Taffard, P. Tornambé, H. Trépanier, X. Zhuang

Editorial Board

[*email:* atlas-SUSY-2015-09-editorial-board@cern.ch]

Jamie Boyd (chair), Sara Strandberg, Kerim Suruliz

ATLAS PAPER

SUSY-2015-09

26th February 2016

Draft version 3.2

Search for supersymmetry at $\sqrt{s} = 13$ TeV in final states with jets and two same-sign leptons or three leptons with the ATLAS detector

The ATLAS Collaboration

Abstract

A search for strongly produced supersymmetric particles is conducted using signatures involving multiple energetic jets and either two isolated leptons (e or μ) with the same electric charge or at least three isolated leptons. The search also utilises b-tagged jets, missing transverse momentum and other observables to extend its sensitivity. The analysis uses a data sample of proton–proton collisions at $\sqrt{s} = 13$ TeV recorded with the ATLAS detector at the Large Hadron Collider in 2015 corresponding to a total integrated luminosity of 3.2 fb^{-1}. No significant excess over the Standard Model expectation is observed. The results are interpreted in several simplified supersymmetric models and extend the exclusion limits from previous searches. In the context of exclusive production and simplified decay modes, gluino masses are excluded at 95% confidence level up to 1.1–1.3 TeV for light neutralinos (depending on the decay channel), and bottom squark masses are also excluded up to 540 GeV. In the former scenarios, neutralino masses are also excluded up to 550-850 GeV for gluino masses around 1 TeV.

To be submitted to: *Eur. Phys. J. C*

1 Introduction

Supersymmetry (SUSY) [1–6] is one of the most studied frameworks to extend the Standard Model (SM) beyond the electroweak scale; a general review can be found in Ref. [7]. In its minimal realisation (MSSM) [8, 9] it predicts a new bosonic (fermionic) partner for each fundamental SM fermion (boson), as well as an additional Higgs doublet. If R-parity is conserved [10] the lightest supersymmetric particle (LSP) is stable and is typically the lightest neutralino[1] $\tilde{\chi}_1^0$. Only such scenarios are considered in this paper. In many models, the LSP can be a viable dark matter candidate [11, 12] and produce collider signatures with large missing transverse momentum.

In order to address the SM hierarchy problem with SUSY models [13–16], TeV-scale masses are required [17, 18] for the partners of the gluons (gluinos $\tilde{g}$) and of the top quark chiral degrees of freedom (top squarks $\tilde{t}_\mathrm{L}$ and $\tilde{t}_\mathrm{R}$), due to the large top Yukawa coupling. The latter also favours significant $\tilde{t}_\mathrm{L}$–$\tilde{t}_\mathrm{R}$ mixing, so that the lighter mass eigenstate $\tilde{t}_1$ is in many scenarios lighter than the other squarks [19, 20]. Bottom squarks may also be light, being bound to top squarks by $SU(2)_\mathrm{L}$ invariance. This leads to potentially large production cross-sections for gluino pairs ($\tilde{g}\tilde{g}$), top–antitop squark pairs ($\tilde{t}_1\tilde{t}_1^*$) and bottom–antibottom squark pairs ($\tilde{b}_1\tilde{b}_1^*$) at the Large Hadron Collider (LHC) [21]. Production of isolated leptons may arise in the cascade decays of those superpartners to SM quarks and neutralinos $\tilde{\chi}_1^0$, via intermediate neutralinos $\tilde{\chi}_{2,3,4}^0$ or charginos $\tilde{\chi}_{1,2}^\pm$ that in turn lead to W, Z or Higgs bosons, or to lepton superpartners (sleptons). Lighter third-generation squarks would also enhance $\tilde{g} \to t\tilde{t}_1^*$ or $\tilde{g} \to b\tilde{b}_1^*$ branching ratios over the generic decays involving light-flavour squarks, favouring the production of heavy flavour quarks and, in the case of top quarks, additional leptons.

This paper presents a search for SUSY in final states with two leptons (electrons or muons) of the same electric charge (referred to as same-sign (SS) leptons) or three leptons (3L) in any charge combination, jets and missing transverse momentum ($\vec{p}_\mathrm{T}^{\,\mathrm{miss}}$, whose magnitude is referred to as $E_\mathrm{T}^\mathrm{miss}$). It is an extension to $\sqrt{s} = 13$ TeV of an earlier search performed by ATLAS with $\sqrt{s} = 8$ TeV data [22], and uses the data collected by the ATLAS experiment [23] in proton–proton (pp) collisions during 2015. Despite the much lower integrated luminosity collected at $\sqrt{s} = 13$ TeV compared to that collected at $\sqrt{s} = 8$ TeV, a similar or improved sensitivity at $\sqrt{s} = 13$ TeV is expected due to the much larger cross-sections predicted for the production of SUSY particles with masses at the TeV scale. A similar search for SUSY in this topology was also performed by the CMS Collaboration [24] at $\sqrt{s} = 8$ TeV. While the same-sign leptons signature is present in many scenarios of physics beyond the SM (BSM), SM processes leading to such final states have very small cross-sections. Compared to many other BSM searches, analyses based on same-sign leptons therefore allow the use of looser kinematic requirements (for example, on $E_\mathrm{T}^\mathrm{miss}$ or the momentum of jets and leptons), preserving sensitivity to scenarios with small mass differences between gluinos/squarks and the LSP, or in which R-parity is not conserved [22].

The sensitivity to a wide range of models is illustrated by the interpretation of the results in the context of four different SUSY benchmark processes that may lead to same-sign or three-lepton signatures. The first two scenarios focus on gluino pair production with generic decays into light quarks and multiple leptons, either involving light sleptons, $\tilde{g} \to q\bar{q}\tilde{\chi}_2^0 \to q\bar{q}\ell\tilde{\ell}^* \to q\bar{q}\ell^+\ell^-\tilde{\chi}_1^0$ (Fig. 1(a)), or mediated by a cascade involving $\tilde{\chi}_1^\pm$ and $\tilde{\chi}_2^0$, $\tilde{g} \to q\bar{q}'\tilde{\chi}_1^\pm \to q\bar{q}'W^\pm\tilde{\chi}_2^0 \to q\bar{q}'W^\pm Z\tilde{\chi}_1^0$ (Fig. 1(b)). The other two scenarios are motivated by the expectation that the third-generation squarks are lighter than the other squarks and target

[1] The SUSY partners of the Higgs and electroweak gauge bosons mix to form the mass eigenstates known as charginos ($\tilde{\chi}_l^\pm$, $l = 1, 2$ ordered by increasing mass) and neutralinos ($\tilde{\chi}_m^0$, $m = 1, \ldots, 4$ ordered by increasing mass).

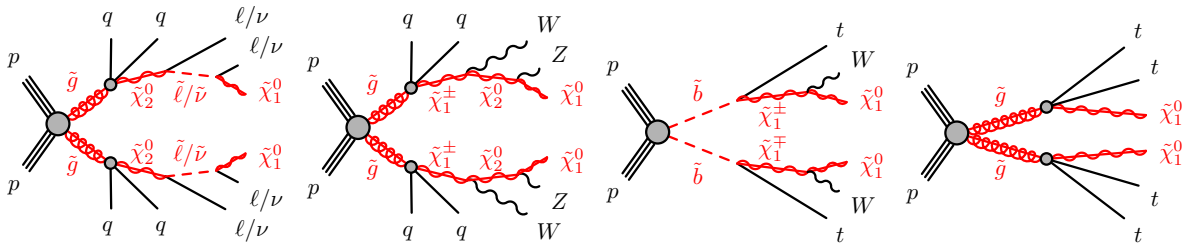

Figure 1: SUSY processes featuring gluino (a, b, d) or bottom squark (c) pair production considered in this analysis.

the direct production of $\tilde{b}_1\tilde{b}_1^*$ pairs with subsequent chargino-mediated $\tilde{b}_1 \to tW^-\tilde{\chi}_1^0$ decays (Fig. 1(c)) or the production of $\tilde{g}\tilde{g}$ pairs decaying as $\tilde{g} \to t\bar{t}\tilde{\chi}_1^0$ via an off-shell top squark (Fig. 1(d)).

Four signal regions (SRs) are designed to achieve good sensitivity for these SUSY scenarios, mainly characterised by the number of b-tagged jets or reconstructed leptons. They are detailed in Section 4, preceded by descriptions of the experimental apparatus (Section 2) and the simulated samples (Section 3). Section 5 is devoted to the estimation of the contribution from SM processes to the signal regions, validated by comparisons with data in dedicated regions. The results are presented in Section 6, together with the statistical tests used to interpret the results in the context of the SUSY benchmark scenarios. Finally, Section 7 summarises the main conclusions of this paper.

2 The ATLAS detector

The ATLAS experiment [23] is a multi-purpose particle detector with a forward-backward symmetric cylindrical geometry and nearly 4π coverage in solid angle.[2] The interaction point is surrounded by an inner detector (ID), a calorimeter system, and a muon spectrometer.

The ID provides precision tracking of charged particles for pseudorapidities $|\eta| < 2.5$ and is surrounded by a superconducting solenoid providing a 2 T axial magnetic field. It consists of pixel and silicon-microstrip detectors inside a transition radiation tracker. One significant upgrade for the $\sqrt{s} = 13$ TeV running period is the presence of the Insertable B-Layer [25], an additional pixel layer close to the interaction point, which provides high-resolution hits at small radius to improve the tracking performance.

In the pseudorapidity region $|\eta| < 3.2$, high-granularity lead/liquid-argon (LAr) electromagnetic (EM) sampling calorimeters are used. A steel/scintillator tile calorimeter measures hadron energies for $|\eta| < 1.7$. The endcap and forward regions, spanning $1.5 < |\eta| < 4.9$, are instrumented with LAr calorimeters for both the EM and hadronic measurements.

[2] ATLAS uses a right-handed coordinate system with its origin at the nominal interaction point (IP) in the centre of the detector and the z-axis along the beam pipe. The x-axis points from the IP to the centre of the LHC ring, and the y-axis points upward. Cylindrical coordinates (r, ϕ) are used in the transverse plane, ϕ being the azimuthal angle around the beam pipe. The pseudorapidity is defined in terms of the polar angle θ as $\eta = -\ln\tan(\theta/2)$. Rapidity is defined as $y = 0.5\ln[(E + p_z)/(E - p_z)]$ where E denotes the energy and p_z is the component of the momentum along the beam direction.

The muon spectrometer consists of three large superconducting toroids with eight coils each, a system of trigger and precision-tracking chambers, which provide triggering and tracking capabilities in the ranges $|\eta| < 2.4$ and $|\eta| < 2.7$, respectively.

A two-level trigger system is used to select events. The first-level trigger is implemented in hardware and uses a subset of the detector information. This is followed by the software-based High-Level Trigger stage, which can run offline reconstruction and calibration software, reducing the event rate to about 1 kHz.

3 Dataset and simulated event samples

The data were collected by the ATLAS detector during 2015 with a peak instantaneous luminosity of $L = 5.2 \times 10^{33}$ cm^{-2}s^{-1}, a bunch spacing of 25 ns, and a mean number of additional pp interactions per bunch crossing (pile-up) in the dataset of $\langle\mu\rangle = 14$. After the application of beam, detector and data quality requirements, the integrated luminosity considered in this analysis corresponds to 3.2 fb^{-1} with an uncertainty of ±5%. The luminosity and its uncertainty are derived following a methodology similar to that detailed in Ref. [26] from a preliminary calibration of the luminosity scale using a pair of x–y beam separation scans performed in August 2015.

Monte Carlo (MC) simulated event samples are used to aid in the estimation of the background from SM processes and to model the SUSY signal. The MC samples are processed through an ATLAS detector simulation [27] based on GEANT4 [28] or a fast simulation using a parameterisation of the calorimeter response and GEANT4 for the other parts of the detector [29] and are reconstructed in the same manner as the data.

Diboson processes with four charged leptons (ℓ), three charged leptons and one neutrino, or two charged leptons and two neutrinos are simulated using the SHERPA v2.1.1 generator [30], and are described in detail in Ref. [31]. The matrix elements contain the doubly resonant WW, WZ and ZZ processes and all other diagrams with four or six electroweak vertices (such as same-electric-charge W boson production in association with two jets, $W^{\pm}W^{\pm}jj$). Fully leptonic triboson processes (WWW, WWZ, WZZ and ZZZ) with up to six charged leptons are also simulated using SHERPA v2.1.1 and described in Ref. [31]. The 4ℓ and $2\ell + 2\nu$ processes are calculated at next-to-leading order (NLO) for up to one additional parton; final states with two and three additional partons are calculated at leading order (LO). The $WWZ \to 4\ell + 2\nu$ or $2\ell + 4\nu$ processes are calculated at LO with up to two additional partons. The $3\ell + 1\nu$ process is calculated at NLO and up to three extra partons at LO using the Comix [32] and OpenLoops [33] matrix element generators and merged with the SHERPA parton shower [34] using the ME+PS@NLO prescription [35]. The $WWZ/WZZ \to 3\ell + 3\nu$, $ZZZ \to 6\ell + 0\nu$, $4\ell + 2\nu$ or $2\ell + 4\nu$ processes are calculated with the same configuration but with up to only two extra partons at LO. The CT10 [36] parton distribution function (PDF) set is used for all SHERPA samples in conjunction with a dedicated tuning of the parton shower parameters developed by the SHERPA authors. The generator cross-sections (at NLO for most of the processes) are used when normalising these backgrounds.

Samples of $t\bar{t}V$ (with $V = W$ and Z, including non-resonant Z/γ^* contributions) and $t\bar{t}WW$ production are generated at LO with MADGRAPH5 v2.2.2 [37] interfaced to the PYTHIA 8.186 [38] parton shower model, with up to two ($t\bar{t}W$), one ($t\bar{t}Z$) or no ($t\bar{t}WW$) extra partons included in the matrix element; they are described in detail in [39]. MADGRAPH5 is also used to simulate the tZ, $t\bar{t}t\bar{t}$ and $t\bar{t}t$ processes. The A14 set of tuned parameters (tune) [40] is used together with the NNPDF23LO PDF set [41]. The $t\bar{t}W$, $t\bar{t}Z$,

$t\bar{t}WW$ and $t\bar{t}t\bar{t}$ events are normalised to their NLO cross-section [42] while the generator cross-section is used for tZ and $t\bar{t}t$.

Production of a Higgs boson in association with a $t\bar{t}$ pair is simulated using aMC@NLO [42] (in MadGraph5 v2.2.2) interfaced to Herwig++ 2.7.1 [43]. The UEEE5 underlying-event tune is used together with the CTEQ6L1 [44] (matrix element) and CT10 [36] (parton shower) PDF sets. Simulated samples of SM Higgs boson production in association with a W or Z boson are produced with Pythia 8.186, using the A14 tune and the NNPDF23LO PDF set. Events are normalised with cross-sections calculated at NLO [45].

The signal SUSY processes are generated from LO matrix elements with up to two extra partons, using the MadGraph5 v2.2.3 generator interfaced to Pythia 8.186 with the A14 tune for the modelling of the SUSY decay chain, parton showering, hadronisation and the description of the underlying event. Parton luminosities are provided by the NNPDF23LO PDF set. Jet–parton matching is realised following the CKKW-L prescription [46], with a matching scale set to one quarter of the pair-produced superpartner mass. Signal cross-sections are calculated to NLO in the strong coupling constant, adding the resummation of soft gluon emission at next-to-leading-logarithmic accuracy (NLO+NLL) [47–51]. The nominal cross-section and the uncertainty are taken from an envelope of cross-section predictions using different PDF sets and factorisation and renormalisation scales, as described in Ref. [52]. The production cross-section of gluino pairs with a mass of 1.2 TeV is 86 fb at $\sqrt{s} = 13$ TeV (compared with 4.4 fb at $\sqrt{s} = 8$ TeV), while the production cross-section of pairs of bottom squarks with a mass of 500 GeV is 520 fb at $\sqrt{s} = 13$ TeV (compared with 86 fb at $\sqrt{s} = 8$ TeV).

In all MC samples, except those produced by Sherpa, the EvtGen v1.2.0 program [53] is used to model the properties of the bottom and charm hadron decays. To simulate the effects of additional pp collisions in the same and nearby bunch crossings, additional interactions are generated using the soft QCD processes of Pythia 8.186 with the A2 tune [54] and the MSTW2008LO PDF [55], and overlaid onto the simulated hard scatter event. The Monte Carlo samples are reweighted so that the distribution of the number of reconstructed vertices matches the distribution observed in the data.

4 Event selection

Candidate events are required to have a reconstructed vertex [56], with at least two associated tracks with $p_{\mathrm{T}} > 400$ MeV, and the vertex with the highest sum of squared transverse momentum of the tracks is considered as primary vertex. In order to perform background estimations using data, two categories of electrons and muons are defined: "candidate" and "signal" (the latter being a subset of the "candidate" leptons satisfying tighter selection criteria).

Electron candidates are reconstructed from an isolated electromagnetic calorimeter energy deposit matched to an ID track and are required to have $|\eta| < 2.47$, a transverse momentum $p_{\mathrm{T}} > 10$ GeV, and to pass a loose likelihood-based identification requirement [57, 58]. The likelihood input variables include measurements of calorimeter shower shapes and measurements of track properties from the ID. Candidates within the transition region between the barrel and endcap electromagnetic calorimeters, $1.37 < |\eta| < 1.52$, are removed. The track matched with the electron must have a significance of the transverse impact parameter with respect to the reconstructed primary vertex, d_0, of $|d_0|/\sigma(d_0) < 5$.

Muon candidates are reconstructed in the region $|\eta| < 2.5$ from muon spectrometer tracks matching ID tracks. All muons must have $p_{\mathrm{T}} > 10$ GeV and must pass the medium identification requirements

defined in Ref. [59], based on selections on the number of hits in the different ID and muon spectrometer subsystems, and the significance of the charge to momentum ratio q/p [59].

Jets are reconstructed with the anti-k_t algorithm [60] with radius parameter $R = 0.4$, using three-dimensional energy clusters in the calorimeter [61] as input. All jets must have $p_{\mathrm{T}} > 20\,\mathrm{GeV}$ and $|\eta| < 2.8$. Jets are calibrated as described in Ref. [62]. In order to reduce the effects of pile-up, for jets with $p_{\mathrm{T}} < 50\,\mathrm{GeV}$ and $|\eta| < 2.4$ a significant fraction of the tracks associated with each jet must have an origin compatible with the primary vertex, as defined by the jet vertex tagger [63]. Furthermore, for all jets the expected average energy contribution from pile-up clusters is subtracted according to the jet area [62].

Identification of jets containing b-hadrons (b-tagging) is performed with the MV2c20 algorithm, a multivariate discriminant making use of track impact parameters and reconstructed secondary vertices [64, 65]. A requirement is chosen corresponding to a 70% average efficiency obtained for b-jets in simulated $t\bar{t}$ events. The rejection factors for light-quark jets, c-quark jets and hadronically decaying τ leptons in simulated $t\bar{t}$ events are approximately 440, 8 and 26, respectively [65]. Jets with $|\eta| < 2.5$ which satisfy this b-tagging requirement are identified as b-jets. To compensate for differences between data and MC simulation in the b-tagging efficiencies and mis-tag rates, correction factors are applied to the simulated samples [65].

After object identification, overlaps between objects are resolved. Any jet within a distance $\Delta R_y = \sqrt{(\Delta y)^2 + (\Delta\phi)^2} = 0.2$ of an electron candidate is discarded, unless the jet has a value of the MV2c20 discriminant larger than the value corresponding to approximately an 80% b-tagging efficiency, in which case the electron is discarded since it is likely originating from a semileptonic b-hadron decay. Any remaining electron within $\Delta R_y = 0.4$ of a jet is discarded. Muons within $\Delta R_y = 0.4$ of a jet are also removed. However, if the jet has fewer than three associated tracks, the muon is kept and the jet is discarded instead to avoid inefficiencies for high-energy muons undergoing significant energy loss in the calorimeter.

Signal electrons must satisfy a tight likelihood-based identification requirement [57, 58] and have $|\eta| < 2$ to reduce the impact of electron charge mis-identification. Signal muons must fulfil the requirement of $|d_0|/\sigma(d_0) < 3$. The track associated to the signal leptons must have a longitudinal impact parameter with respect to the reconstructed primary vertex, z_0, satisfying $|z_0 \sin\theta| < 0.5$ mm. Isolation requirements are applied to both the signal electrons and muons. The scalar sum of the p_{T} of tracks within a variable-size cone around the lepton, excluding its own track, must be less than 6% of the lepton p_{T}. The track isolation cone radius for electrons (muons) $\Delta R_\eta = \sqrt{(\Delta\eta)^2 + (\Delta\phi)^2}$ is given by the smaller of $\Delta R_\eta = 10\ \mathrm{GeV}/p_{\mathrm{T}}$ and $\Delta R_\eta = 0.2\,(0.3)$, that is, a cone of size $0.2\,(0.3)$ at low p_{T} but narrower for high-p_{T} leptons. In addition, in the case of electrons the energy of calorimeter energy clusters in a cone of $\Delta R_\eta = 0.2$ around the electron (excluding the deposition from the electron itself) must be less than 6% of the electron p_{T}. Simulated events are corrected to account for minor differences in the lepton trigger, reconstruction and identification efficiencies between data and MC simulation.

The missing transverse momentum $\vec{p}_{\mathrm{T}}^{\,\mathrm{miss}}$ is defined as the negative vector sum of the transverse momenta of all identified physics objects (electrons, photons, muons, jets) and an additional soft term. The soft term is constructed from all tracks that are not associated with any physics object, and that are associated with the primary vertex. In this way, the $E_{\mathrm{T}}^{\mathrm{miss}}$ is adjusted for the best calibration of the jets and the other identified physics objects above, while maintaining pile-up independence in the soft term [66, 67].

Events are selected using a combination (logical OR) of dilepton and $E_{\mathrm{T}}^{\mathrm{miss}}$ triggers, the latter being used only for events with $E_{\mathrm{T}}^{\mathrm{miss}} > 250\,\mathrm{GeV}$. The trigger-level requirements on $E_{\mathrm{T}}^{\mathrm{miss}}$ and the leading and subleading lepton p_{T} are looser than those applied offline to ensure that trigger efficiencies are constant in the relevant phase space. Events of interest are selected if they contain at least two signal leptons with $p_{\mathrm{T}} > 20$ GeV. If the event contains exactly two signal leptons, they are required to have the same electric charge.

To maximise the sensitivity in different signal models, four overlapping signal regions are defined as shown in Table 1, with requirements on the number of signal leptons ($N_{\mathrm{lept}}^{\mathrm{signal}}$), the number of b-jets with $p_{\mathrm{T}} > 20\,\mathrm{GeV}$ ($N_{b-\mathrm{jets}}^{20}$), the number of jets with $p_{\mathrm{T}} > 50\,\mathrm{GeV}$ regardless of their flavour (N_{jets}^{50}), $E_{\mathrm{T}}^{\mathrm{miss}}$ and the effective mass (m_{eff}), defined as the scalar sum of the p_{T} of the signal leptons and jets (regardless of their flavour) in the event plus the $E_{\mathrm{T}}^{\mathrm{miss}}$.

Table 1: Summary of the event selection criteria for the signal regions (see text for details).

Signal region	$N_{\mathrm{lept}}^{\mathrm{signal}}$	$N_{b-\mathrm{jets}}^{20}$	N_{jets}^{50}	$E_{\mathrm{T}}^{\mathrm{miss}}$ [GeV]	m_{eff} [GeV]
SR0b3j	≥3	=0	≥3	>200	>550
SR0b5j	≥2	=0	≥5	>125	>650
SR1b	≥2	≥1	≥4	>150	>550
SR3b	≥2	≥3	-	>125	>650

Each signal region is motivated by a different SUSY scenario. The SR0b3j and SR0b5j signal regions are sensitive to gluino-mediated and directly produced squarks of the first and second generations leading to final states particularly rich in leptons (Fig. 1(a)) or in jets (Fig. 1(b)), but with no enhancement of the production of b-quarks. Third-generation squark models resulting in final states with two b-quarks, such as direct bottom squark production (Fig. 1(c)), are targeted by the SR1b signal region. Finally, the signal region SR3b targets gluino-mediated top squark production resulting in final states with four b-quarks (Fig. 1(d)).

The values of acceptance times efficiency of the SR selections for the SUSY signal models in Fig. 1 typically range between 1% and 6% for $m_{\tilde{g}} = 1.2\,\mathrm{TeV}$ or $m_{\tilde{b}_1} = 600\,\mathrm{GeV}$, and a light $\tilde{\chi}_1^0$.

5 Background estimation

Three main sources of SM background can be distinguished in this analysis. A first category consists of events with two same-sign prompt leptons or at least three prompt leptons, mainly from $t\bar{t}V$ and diboson processes. Other types of background events include those containing electrons with mis-measured charge, mainly from the production of top quark pairs, and those containing at least one non-prompt or fake lepton, which mainly originate from hadron decays in events containing top quarks or of W bosons in association with jets.

5.1 Background estimation methods

The estimation of the SM background processes with two same-sign prompt leptons or at least three prompt leptons is performed using the MC samples described in Section 3. Since diboson and $t\bar{t}V$ events are the main backgrounds in the signal regions, dedicated validation regions with an enhanced contribution from these processes are defined to verify the background predictions (see Section 5.3).

Background events due to charge mis-identification, dominated by electrons having emitted a hard bremsstrahlung photon which subsequently converted to an electron–positron pair, are referred to as "charge-flip". The probability of mis-identifying the charge of a muon is checked in both data and MC simulation, and found to be negligible in the kinematic range relevant to this analysis. The contribution of charge-flip events is estimated using data. The electron charge-flip probability is extracted in a $Z/\gamma^* \rightarrow ee$ data sample using a likelihood fit which takes as input the numbers of same-sign and opposite-sign electron pairs observed in the sample. The charge-flip probability is a free parameter of the fit and is extracted as a function of the electron p_{T} and η. The event yield of this background in the signal or validation regions is obtained by applying the measured charge-flip probability to data regions with the same kinematic requirements as the signal or validation regions but with opposite-sign lepton pairs.

The contribution from fake or non-prompt (FNP) leptons (such as hadrons mis-identified as leptons, leptons originating from heavy-flavour decays, and electrons from photon conversions) is also estimated from data with a matrix method similar to that described in Ref. [22]. In this method, two types of lepton identification criteria are defined: "tight", corresponding to the signal lepton criteria described in Section 4, and "loose", corresponding to candidate leptons. The matrix method relates the number of events containing prompt or FNP leptons to the number of observed events with tight or loose-not-tight leptons using the probability for loose prompt or FNP leptons to satisfy the tight criteria. The probability for loose prompt leptons to satisfy the tight selection criteria is obtained using a $Z/\gamma^* \rightarrow \ell\ell$ data sample and is modelled as a function of the lepton p_{T} and η. The probability for loose FNP leptons to satisfy the tight selection criteria is determined from data in a SS control region enriched in non-prompt leptons originating from heavy-flavour decays. This region contains events with at least one b-jet, one tight muon with $p_{\mathrm{T}} > 40$ GeV (likely prompt) and an additional loose electron or muon (likely FNP). The contribution from prompt leptons and charge mis-measured electrons to this region is subtracted from the observed event yields.

The data-driven background estimates are cross-checked with an MC-based technique. In this method, the contributions from processes with FNP leptons and electron charge mis-identification are obtained from MC simulation and normalised to data in dedicated control regions at low jet multiplicity, low $E_{\mathrm{T}}^{\mathrm{miss}}$, and either with or without b-jets. The normalisation is performed using five multipliers: one to correct the electron charge mis-identification rate, and four to correct the contributions from FNP electrons or muons originating from b-jets or light-flavour jets, respectively. In addition to the MC samples listed in Section 3, this method employs samples of top quark pair production generated with the Powheg-Box v2 generator interfaced to Pythia 6.428 [68], as well as samples of simulated W+jets and Z+jets events generated with Powheg-Box v2 interfaced to Pythia 8.186.

5.2 Systematic uncertainties on the background estimation

Table 2 summarises the contributions of the different sources of systematic uncertainty in the total SM background predictions in the signal regions.

The systematic uncertainties related to the same-sign prompt leptons background estimation arise from the accuracy of the theoretical and experimental modelling in the MC simulation. The primary sources of systematic uncertainties are related to the jet energy scale calibration, the jet energy resolution, b-tagging efficiency, and MC modelling and theoretical cross-section uncertainties. The cross-sections used to normalise the MC samples are varied according to the uncertainty in the cross-section calculation, that is, 6% for diboson, 13% for $t\bar{t}W$ and 12% $t\bar{t}Z$ production [42]. Additional uncertainties are assigned to these backgrounds to account for the modelling of the kinematic distributions in the MC simulation. For $t\bar{t}W$ and $t\bar{t}Z$, the predictions from the MadGraph5 and Sherpa generators are compared, leading to a ~30% uncertainty for these processes after the SR selections. For dibosons, uncertainties are estimated by varying the renormalisation, factorisation and resummation scales used to generate these samples, leading to a ~30% uncertainty for these processes after the SR selections. For triboson, $t\bar{t}h$, $t\bar{t}t\bar{t}$ and tZ production processes, which constitute a small background in all signal regions, a 50% uncertainty on the event yields is assumed.

Uncertainties in the FNP lepton background estimate are assigned due to the limited number of data events with loose and tight leptons. In addition, systematic uncertainties of 50–60% are assigned to the probabilities for loose FNP leptons to satisfy the tight signal criteria to account for potentially different FNP compositions (heavy flavour, light flavour or conversions) between the regions used to measure these probabilities and the SRs, as well as the contamination from prompt leptons in the former regions. This leads to overall FNP background uncertainties in the total background estimates of 18–21% depending on the signal region.

For the charge-flip background prediction, the main uncertainties originate from the statistical uncertainty of the charge-flip probability measurements and the background contamination of the sample used to extract the charge-flip probability.

Table 2: The main sources of systematic uncertainty on the SM background estimates for the four signal regions are shown and their values given as relative uncertainties in the expected signal region background event yields. The individual components can be correlated and therefore do not necessarily add up in quadrature to the total systematic uncertainty. For reference, the total number of expected background events is also shown.

	SR0b3j	SR0b5j	SR1b	SR3b
Diboson theoretical uncertainties	23%	16%	1%	<1%
$t\bar{t}V$ theoretical uncertainties	3%	4%	13%	9%
Other theoretical uncertainties	5%	3%	9%	15%
MC statistical uncertainties	11%	14%	3%	6%
Jet energy scale	12%	11%	6%	5%
Jet energy resolution	3%	9%	2%	3%
b-tagging	4%	6%	3%	10%
PDF	6%	6%	6%	8%
Fake/non-prompt leptons	18%	20%	18%	21%
Charge flip	–	1%	3%	8%
Total background uncertainties	30%	34%	22%	31%
Total background events	1.5	0.88	4.5	0.80

Table 3: Summary of the event selection in the validation regions. Requirements are placed on the number of signal leptons ($N_{\text{lept}}^{\text{signal}}$) and candidate leptons ($N_{\text{lept}}^{\text{cand}}$), the number of jets with $p_{\text{T}} > 25\,\text{GeV}$ (N_{jets}^{25}) or the number of b-jets with $p_{\text{T}} > 20\,\text{GeV}$ ($N_{b-\text{jets}}^{20}$). The three leading-p_{T} leptons are referred to as $\ell_{1,2,3}$ with decreasing p_{T} and the two leading jets as $j_{1,2}$. Additional requirements are set on the invariant mass of the two leading electrons m_{ee}, the presence of SS leptons or a pair of same-flavour opposite-sign leptons (SFOS) and its invariant mass m_{SFOS}.

	$N_{\text{lept}}^{\text{signal}}$ ($N_{\text{lept}}^{\text{cand}}$)	$N_{b-\text{jets}}^{20}$	N_{jets}^{25}	$E_{\text{T}}^{\text{miss}}$ [GeV]	m_{eff} [GeV]	Other
VR-WW	=2 (=2) =1 SS pair	=0	≥2	35–200	300–900	$m(j_1 j_2) > 500$ GeV $p_{\text{T}}(j_2) > 40$ GeV $p_{\text{T}}(\ell_2) > 30$ GeV veto $80 < m_{ee} < 100$ GeV
VR-WZ	=3 (=3)	=0	1–3	30–200	<900	$p_{\text{T}}(\ell_3) > 30$ GeV
VR-ttV	≥2 (-) ≥1 SS pair	≥2	≥5 ($e^{\pm}e^{\pm}$,$e^{\pm}\mu^{\pm}$) ≥3 ($\mu^{\pm}\mu^{\pm}$)	20–200	200–900	$p_{\text{T}}(\ell_2) > 25$ GeV veto $\{E_{\text{T}}^{\text{miss}} > 125$ and $m_{\text{eff}} > 650\,\text{GeV}\}$
VR-ttZ	≥3 (-) ≥1 SFOS pair	≥1	≥4 (=1 b-jet) ≥3 (≥2 b-jets)	20–150	100–900	$p_{\text{T}}(\ell_2) > 25$ GeV $p_{\text{T}}(\ell_3) > 20$ GeV (if e) $80 < m_{\text{SFOS}} < 100$ GeV
All VRs	Veto events belonging to any SR, or if ℓ_1 or ℓ_2 is an electron with $\lvert\eta\rvert > 1.37$ (except in VR-WZ)					

5.3 Validation of background estimates

To check the validity and robustness of the background estimates, the distributions of several discriminating variables in data are compared with the predicted background after various requirements on the number of jets and b-jets. Events are categorised based on the flavours of the selected leptons, and the different flavour channels are compared separately. Examples of such distributions are shown in Fig. 2(a)–2(c) and illustrate that the predictions and data agree fairly well. The background estimates in a kinematic region close to the signal regions can also be observed in Fig. 3, which shows the $E_{\text{T}}^{\text{miss}}$ distributions in the signal regions before applying the $E_{\text{T}}^{\text{miss}}$ requirements.

Dedicated validation regions (VRs) are defined to test the estimate of the rare SM processes contributing to the signal regions, whose cross-sections have not yet been measured at $\sqrt{s} = 13$ TeV. The corresponding selections are summarised in Table 3. In these regions, upper bounds are placed on $E_{\text{T}}^{\text{miss}}$ and m_{eff} to reduce signal contamination, and the small residual overlap with the signal regions is resolved by vetoing events that contribute to the signal regions. To further reduce contributions from electron charge mis-identification, events are also vetoed if one of the two leading leptons is an electron with $\lvert\eta\rvert > 1.37$, since contributions from charge-flip electrons are smaller in the central region due to the lower amount of crossed material. The purity of the targeted processes in these regions ranges from about 40% to 80%. The VR-ttV and VR-ttZ regions overlap with each other, with 30% of the $t\bar{t}V$ events in VR-ttV also present in VR-ttZ, and the contributions from the $t\bar{t}Z$ and $t\bar{t}W$ processes is similar in VR-ttV.

The observed yields in these validation regions, compared with the background predictions and uncertainties, can be seen in Table 4, and the effective mass distributions are shown in Fig. 2(d)–2(f). There is fair agreement between data and the estimated background for the validation regions, with the largest deviations being observed in VR-ttV with a 1.5σ deviation.

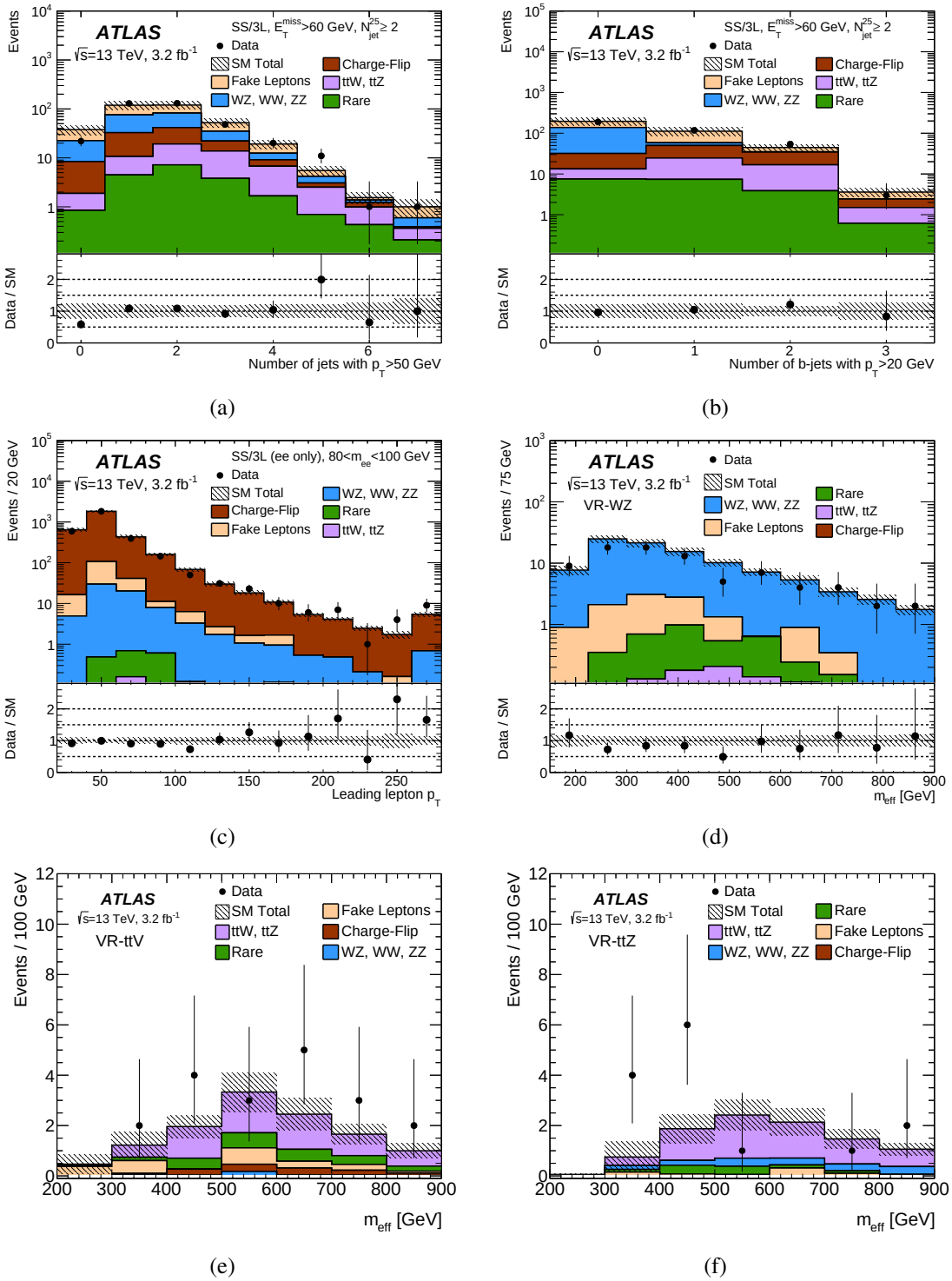

Figure 2: Distributions of kinematic variables after a SS/3L selection including (a), (b) $E_{\mathrm{T}}^{\mathrm{miss}} > 60\,\mathrm{GeV}$ and $N_{\mathrm{jet}}^{25} \geq 2$, (c) a b-jet veto and $80 < m_{\ell\ell} < 100\,\mathrm{GeV}$, and (d), (e), (f) distributions in the validation regions. The statistical uncertainties in the background prediction are included in the uncertainty band, as well as the theory uncertainties for the backgrounds with prompt SS/3L, and the full systematic uncertainties for data-driven backgrounds. The last bin includes overflows. The "Fake leptons" category corresponds to FNP leptons (see text), and the "Rare" category contains the contributions from associated production of $t\bar{t}$ with $h/WW/t/t\bar{t}$, as well as tZ, Wh, Zh, and triboson production. The lower part of the figures (a)–(d) shows the ratio of data to the background prediction.

Table 4: The numbers of observed data and expected background events for the validation regions. The "Rare" category contains the contributions from associated production of $t\bar{t}$ with $h/WW/t/t\bar{t}$, as well as tZ, Wh, Zh, and triboson production. Background categories shown as "–" denote that they cannot contribute to a given region (charge flips or $W^{\pm}W^{\pm}jj$ in 3-lepton regions). The individual uncertainties can be correlated and therefore do not necessarily add up in quadrature to the total systematic uncertainty.

	VR-WW	VR-WZ	VR-ttV	VR-ttZ
Observed events	4	82	19	14
Total background events	3.4 ± 0.8	98 ± 15	12.1 ± 2.7	9.7 ± 2.5
Fake/non-prompt leptons	0.6 ± 0.5	8 ± 6	2.1 ± 1.4	0.6 ± 1.0
Charge-flip	0.26 ± 0.05	–	1.14 ± 0.15	–
$t\bar{t}W$	0.05 ± 0.03	0.25 ± 0.09	2.4 ± 0.8	0.10 ± 0.03
$t\bar{t}Z$	0.02 ± 0.01	0.72 ± 0.26	3.9 ± 1.3	6.3 ± 2.1
WZ	1.0 ± 0.4	78 ± 13	0.19 ± 0.10	1.2 ± 0.4
$W^{\pm}W^{\pm}jj$	1.3 ± 0.5	–	0.02 ± 0.03	–
ZZ	0.02 ± 0.01	8.2 ± 2.8	0.12 ± 0.15	0.30 ± 0.19
Rare	0.10 ± 0.05	2.8 ± 1.4	2.3 ± 1.2	1.1 ± 0.6

Table 5: The number of observed data events and expected background contributions in the signal regions. The p-value of the observed events for the background-only hypothesis is denoted by $p(s = 0)$. The "Rare" category contains the contributions from associated production of $t\bar{t}$ with $h/WW/t/t\bar{t}$, as well as tZ, Wh, Zh, and triboson production. Background categories shown as "–" denote that they cannot contribute to a given region (charge flips or $W^{\pm}W^{\pm}jj$ in 3-lepton regions). The individual uncertainties can be correlated and therefore do not necessarily add up in quadrature to the total systematic uncertainty.

	SR0b3j	SR0b5j	SR1b	SR3b
Observed events	3	3	7	1
Total background events	1.5 ± 0.4	0.88 ± 0.29	4.5 ± 1.0	0.80 ± 0.25
$p(s = 0)$	0.13	0.04	0.15	0.36
Fake/non-prompt leptons	< 0.2	0.05 ± 0.18	0.8 ± 0.8	0.13 ± 0.17
Charge-flip	–	0.02 ± 0.01	0.60 ± 0.12	0.19 ± 0.06
$t\bar{t}W$	0.02 ± 0.01	0.08 ± 0.04	1.1 ± 0.4	0.10 ± 0.05
$t\bar{t}Z$	0.10 ± 0.04	0.05 ± 0.03	0.92 ± 0.31	0.14 ± 0.06
WZ	1.2 ± 0.4	0.48 ± 0.20	0.18 ± 0.11	< 0.02
$W^{\pm}W^{\pm}jj$	–	0.12 ± 0.07	0.03 ± 0.02	< 0.01
ZZ	< 0.03	< 0.04	< 0.03	< 0.03
Rare	0.14 ± 0.08	0.07 ± 0.05	0.8 ± 0.4	0.24 ± 0.14

6 Results

Figure 3 shows the data $E_{\mathrm{T}}^{\mathrm{miss}}$ distributions after the signal region selections (beside that on $E_{\mathrm{T}}^{\mathrm{miss}}$) in data together with the expected contributions from all the SM backgrounds with their total statistical and

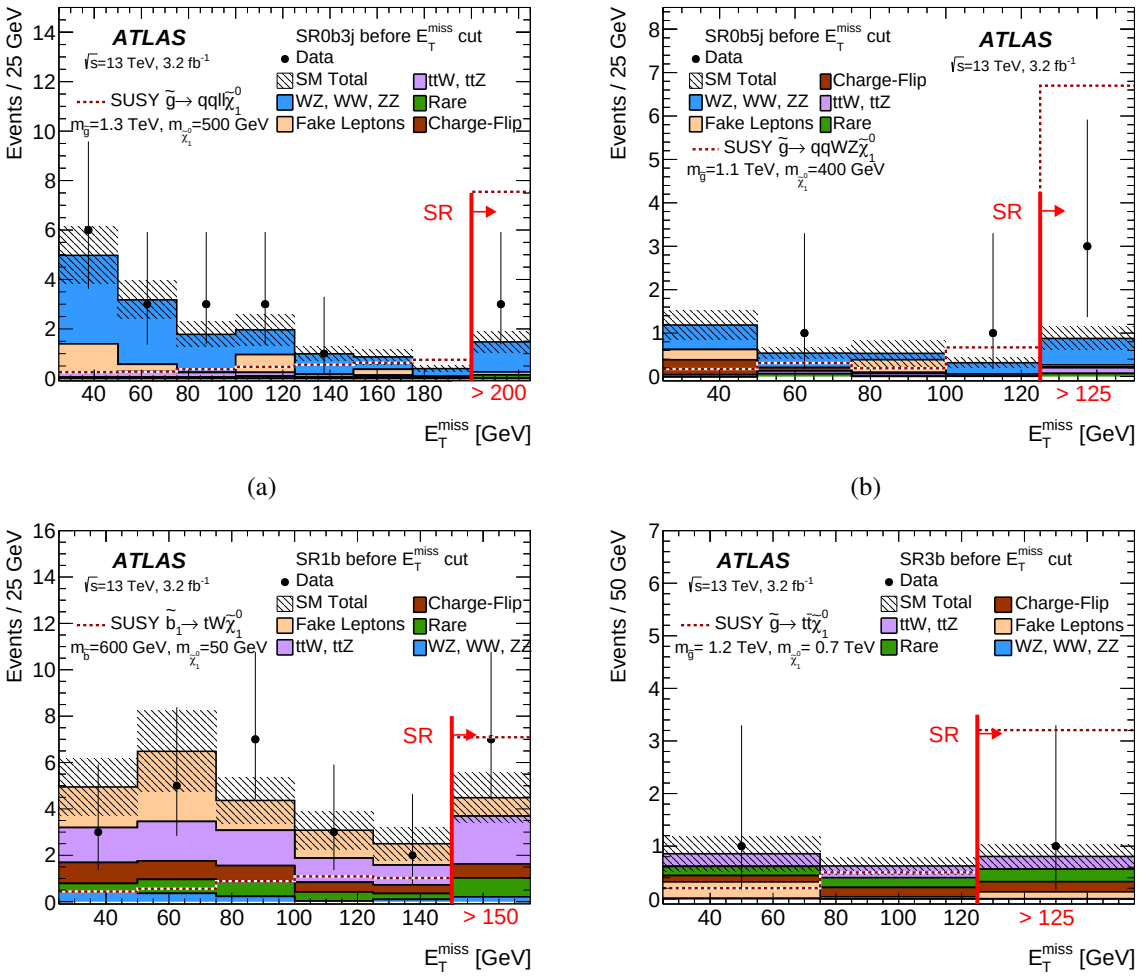

Figure 3: Missing transverse momentum distributions after (a) SR0b3j, (b) SR0b5j, (c) SR1b and (d) SR3b selection, beside the $E_{\mathrm{T}}^{\mathrm{miss}}$ requirement. The results in the signal regions are shown in the last (inclusive) bin of each plot. The statistical uncertainties in the background prediction are included in the uncertainty band, as well as the theory uncertainties for the backgrounds with prompt SS/3L, and the full systematic uncertainties for data-driven backgrounds. The "Fake leptons" category corresponds to FNP leptons (see text), and the "Rare" category contains the contributions from associated production of $t\bar{t}$ with $h/WW/t/t\bar{t}$, as well as tZ, Wh, Zh, and triboson production.

systematic uncertainties. For illustration, a typical SUSY signal distribution corresponding to the most relevant benchmark scenario in each SR is displayed. The detailed yields for data and the different sources of SM background in the signal regions are presented in Table 5. The uncertainties amount to 22–34% of the total background depending on the signal region. In all four SRs the number of data events exceeds the expectation but is consistent within the uncertainties, the smallest p-value for the SM-only hypothesis being 0.04 for SR0b5j. Out of the 14 events in the SRs, 2 of the events in SR1b and the 3 events in SR0b3j contain three leptons. None of those events contain three leptons of equal charge.

In the absence of any significant deviations from the SM predictions, upper limits on possible BSM contributions to the signal regions are computed, in particular in the context of the SUSY benchmark scenarios described in Section 1. The HistFitter framework [69], which utilises a profile-likelihood-ratio

test [70], is used to establish 95% confidence intervals using the CL_s prescription [71]. The likelihood is built as the product of a Poisson probability density function describing the observed number of events in the signal region and Gaussian distributions constraining the nuisance parameters associated with the systematic uncertainties whose widths correspond to the sizes of these uncertainties; Poisson distributions are used instead for MC statistical uncertainties. Correlations of a given nuisance parameter across the different sources of backgrounds and the signal are taken into account when relevant. The statistical tests are performed independently for each of the signal regions.

Table 6 presents 95% confidence level (CL) model-independent upper limits on the number of BSM events, N_{BSM}, that may contribute to the signal regions. Normalising these by the integrated luminosity L of the data sample, they can be interpreted as upper limits on the visible BSM cross-section σ_{vis}, defined as the product $\sigma_{\text{prod}} \times A \times \epsilon = N_{\text{BSM}}/L$ of production cross-section, acceptance and reconstruction efficiency.

Table 6: Signal model-independent upper limits on the number of BSM events (N_{BSM}) and the visible signal cross-section (σ_{vis}) in the four SRs. The numbers (in parentheses) give the observed (expected under the SM hypothesis) 95% CL upper limits. Calculations are performed with pseudo-experiments. The $\pm 1\sigma$ variations on the expected limit due to the statistical and systematic uncertainties in the background prediction are also shown.

	SR0b3j	SR0b5j	SR1b	SR3b
$N_{\text{BSM}}^{\text{obs}}$ ($N_{\text{BSM}}^{\text{exp}}$)	5.9 ($4.1^{+1.6}_{-0.8}$)	6.4 ($3.6^{+1.2}_{-1.1}$)	8.8 ($6.0^{+2.6}_{-1.6}$)	3.8 ($3.7^{+1.1}_{-0.5}$)
$\sigma_{\text{vis}}^{\text{obs}}$ [fb]	1.8	2.0	2.8	1.2

Exclusion limits are also set on the masses of the superpartners involved in the four SUSY benchmark scenarios considered in this analysis. Simplified models corresponding to a single production mode and with 100% branching ratio to a specific decay chain are used, with the masses of the SUSY particles not involved in the process set to very high values. Figure 4 shows the limits on the mass of the $\tilde{\chi}_1^0$ as a function of the $\tilde{g}$ or $\tilde{b}_1$ mass. In some cases, the new limits set by this analysis can be compared with the existing limits set by the combination of ATLAS SUSY searches with 8 TeV data [72, 73]. For parts of the parameter space, the sensitivity reached with the 13 TeV dataset exceeds that of the 8 TeV dataset, and additional parameter space regions can be excluded, especially for large neutralino masses.

Signal models featuring gluino pair production with a subsequent gluino decay via $\tilde{\chi}_2^0$ and light sleptons ($\tilde{g} \to q\bar{q}\tilde{\chi}_2^0 \to q\bar{q}(\ell\tilde{\ell}^*/\nu\tilde{\nu}^*) \to q\bar{q}(\ell^+\ell^-/\nu\nu)\tilde{\chi}_1^0$) are probed using SR0b3j (Fig. 4(a)). In this simplified model, the gluinos decay into $u\bar{u}$, $d\bar{d}$, $s\bar{s}$ or $c\bar{c}$ with equal probabilities, and the six types of leptons are also produced in the $\tilde{\chi}_2^0$ decays with equal probabilities. The $\tilde{\chi}_2^0$ mass is set to $m_{\tilde{\chi}_2^0} = (m_{\tilde{g}} + m_{\tilde{\chi}_1^0})/2$, with the $\tilde{\ell}$ and $\tilde{\nu}$ masses set to $m_{\tilde{\ell},\tilde{\nu}} = (m_{\tilde{\chi}_2^0} + m_{\tilde{\chi}_1^0})/2$. Gluino masses up to $m_{\tilde{g}} \approx 1.3\,\text{TeV}$ for a light $\tilde{\chi}_1^0$ and $\tilde{\chi}_1^0$ masses up to $m_{\tilde{\chi}_1^0} \approx 850\,\text{GeV}$ for gluinos with $m_{\tilde{g}} \approx 1.1\,\text{TeV}$ are excluded in this scenario.

Similarly, models with gluino production with a subsequent two-step gluino decay via $\tilde{\chi}_1^\pm$ and $\tilde{\chi}_2^0$ ($\tilde{g} \to q\bar{q}\tilde{\chi}_1^\pm \to q\bar{q}W\tilde{\chi}_2^0 \to q\bar{q}WZ\tilde{\chi}_1^0$) are probed with SR0b5j (Fig. 4(b)). In this simplified model, the gluinos decay into $u\bar{u}$, $d\bar{d}$, $s\bar{s}$ or $c\bar{c}$ with equal probabilities. The $\tilde{\chi}_1^\pm$ mass is set to $m_{\tilde{\chi}_1^\pm} = (m_{\tilde{g}} + m_{\tilde{\chi}_1^0})/2$ and the $\tilde{\chi}_2^0$ mass is set to $m_{\tilde{\chi}_2^0} = (m_{\tilde{\chi}_1^\pm} + m_{\tilde{\chi}_1^0})/2$; W and Z bosons produced in the decay chain are not necessarily on-shell. The exclusion limits in this scenario reach $m_{\tilde{g}} \approx 1.1\,\text{TeV}$ (for light $\tilde{\chi}_1^0$) and $m_{\tilde{\chi}_1^0} \approx 550\,\text{GeV}$ (for $m_{\tilde{g}} \approx 1.0\,\text{TeV}$).

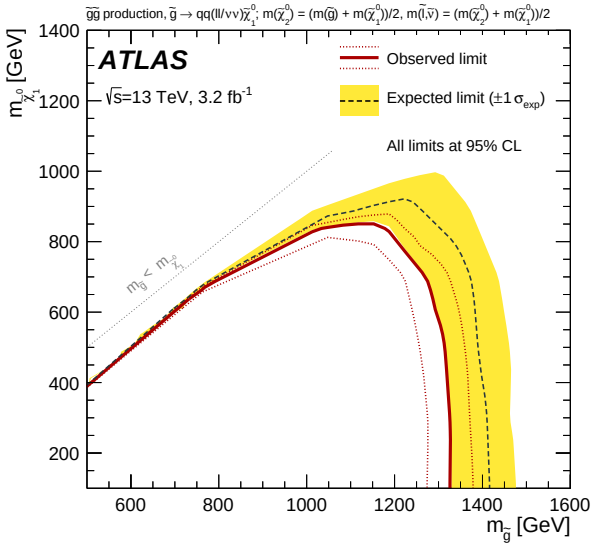

(a) $\tilde{g} \rightarrow q\bar{q}\ell\ell\tilde{\chi}_1^0$ scenario, SR0b3j

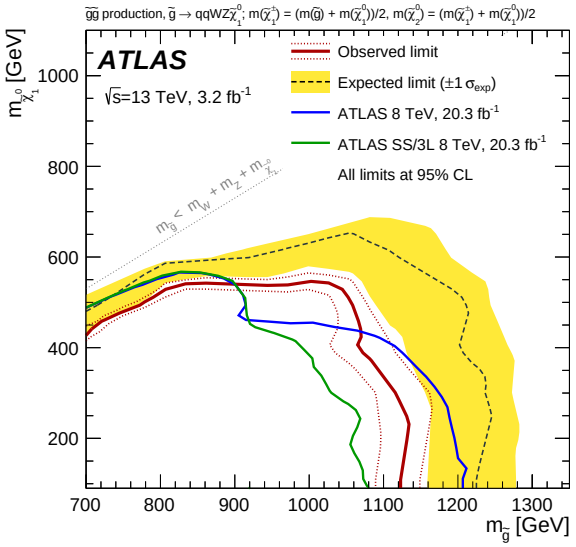

(b) $\tilde{g} \rightarrow q\bar{q}'WZ\tilde{\chi}_1^0$ scenario, SR0b5j

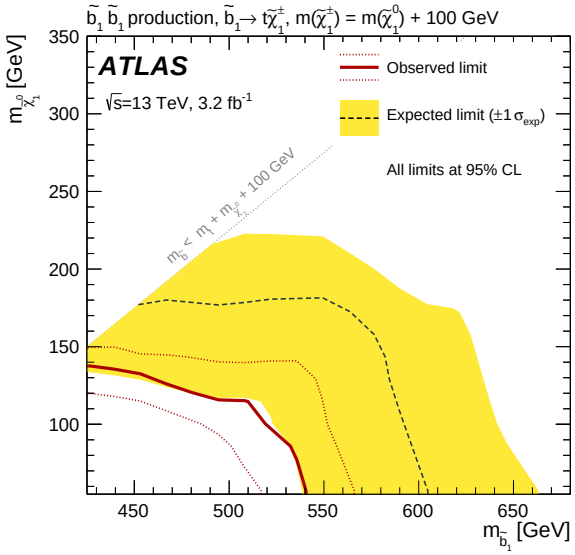

(c) $\tilde{b}_1 \rightarrow tW^-\tilde{\chi}_1^0$ scenario, SR1b

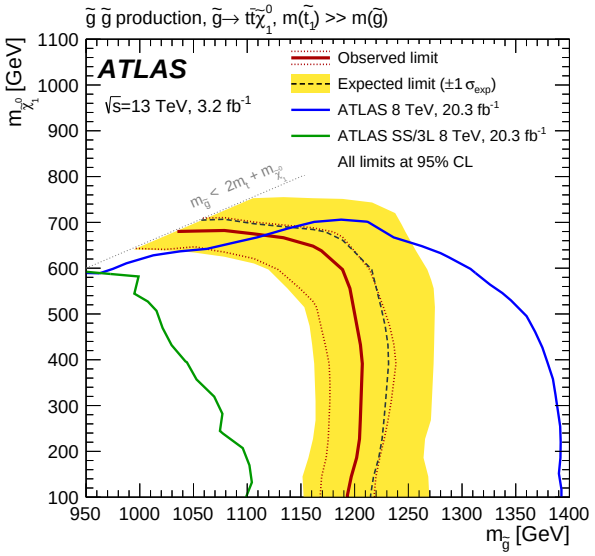

(d) $\tilde{g} \rightarrow t\bar{t}\tilde{\chi}_1^0$ scenario, SR3b

Figure 4: Observed and expected exclusion limits on the $\tilde{g}$, $\tilde{b}_1$and $\tilde{\chi}_1^0$ masses in the context of SUSY scenarios with simplified mass spectra featuring $\tilde{g}\tilde{g}$ or $\tilde{b}_1\tilde{b}_1^*$ pair production with exclusive decay modes. The signal region used to obtain the limits is specified for each scenario. The contours of the band around the expected limit are the $\pm 1\sigma$ results, including all uncertainties except theoretical uncertainties on the signal cross-section. The dotted lines around the observed limit illustrate the change in the observed limit as the nominal signal cross-section is scaled up and down by the theoretical uncertainty. All limits are computed at 95% CL. The diagonal lines indicate the kinematic limit for the decays in each specified scenario. For figures (b) and (d), results are compared with the observed limits obtained by previous ATLAS searches [22, 72, 73]. For figures (a) and (c), a direct comparison with earlier searches is not possible, due to differing model assumptions.

Exclusion limits in a simplified model of bottom squark production with chargino-mediated $\tilde{b}_1 \to tW^-\tilde{\chi}_1^0$ decays are obtained with SR1b (Fig. 4(c)). In this model the $\tilde{\chi}_1^\pm$ mass is set to $m_{\tilde{\chi}_1^\pm} = m_{\tilde{\chi}_1^0} + 100\,\text{GeV}$. The limits can reach mass values of $m_{\tilde{b}_1} \approx 540\,\text{GeV}$ for a light $\tilde{\chi}_1^0$, while $m_{\tilde{\chi}_1^0} \lesssim 140\,\text{GeV}$ are also excluded for $m_{\tilde{b}_1} \approx 425\,\text{GeV}$, significantly extending the previous limits obtained at $\sqrt{s} = 8$ TeV [73] which excluded $m_{\tilde{b}_1} \lesssim 470\,\text{GeV}$ for $m_{\tilde{\chi}_1^0} \approx 60\,\text{GeV}$ for a similar model.

Finally, SR3b is used to set limits on masses in a simplified model with gluino pair production and $\tilde{g} \to t\bar{t}\tilde{\chi}_1^0$ decays via an off-shell top squark (Fig. 4(d)). In that case, gluino masses of $m_{\tilde{g}} \lesssim 1.2\,\text{TeV}$ are excluded for $m_{\tilde{\chi}_1^0} \lesssim 600\,\text{GeV}$, and $\tilde{\chi}_1^0$ masses up to $m_{\tilde{\chi}_1^0} \approx 680\,\text{GeV}$ are also excluded for $m_{\tilde{g}} \approx 1.05\,\text{TeV}$.

7 Conclusion

A search for supersymmetry in events with exactly two same-sign leptons or at least three leptons, multiple jets, b-jets and $E_{\text{T}}^{\text{miss}}$ is presented. The analysis is performed with proton–proton collision data at $\sqrt{s} = 13$ TeV collected with the ATLAS detector at the Large Hadron Collider corresponding to an integrated luminosity of 3.2 fb^{-1}. With no significant excess over the Standard Model expectation observed, results are interpreted in the framework of simplified models featuring gluino and bottom squark production. In the $\tilde{g}\tilde{g}$ simplified models considered, $m_{\tilde{g}} \lesssim 1.1$–$1.3$ TeV and $m_{\tilde{\chi}_1^0} \lesssim 550$–$850$ GeV are excluded at 95% confidence level depending on the model parameters. Bottom squark masses of $m_{\tilde{b}_1} \lesssim 540$ GeV are also excluded for a light $\tilde{\chi}_1^0$ in a $\tilde{b}_1\tilde{b}_1^*$ simplified model with $\tilde{b}_1 \to tW^-\tilde{\chi}_1^0$. These results are complementary to those of previous searches and extend the exclusion limits they set.

Acknowledgements

We thank CERN for the very successful operation of the LHC, as well as the support staff from our institutions without whom ATLAS could not be operated efficiently.

We acknowledge the support of ANPCyT, Argentina; YerPhI, Armenia; ARC, Australia; BMWFW and FWF, Austria; ANAS, Azerbaijan; SSTC, Belarus; CNPq and FAPESP, Brazil; NSERC, NRC and CFI, Canada; CERN; CONICYT, Chile; CAS, MOST and NSFC, China; COLCIENCIAS, Colombia; MSMT CR, MPO CR and VSC CR, Czech Republic; DNRF, DNSRC and Lundbeck Foundation, Denmark; IN2P3-CNRS, CEA-DSM/IRFU, France; GNSF, Georgia; BMBF, HGF, and MPG, Germany; GSRT, Greece; RGC, Hong Kong SAR, China; ISF, I-CORE and Benoziyo Center, Israel; INFN, Italy; MEXT and JSPS, Japan; CNRST, Morocco; FOM and NWO, Netherlands; RCN, Norway; MNiSW and NCN, Poland; FCT, Portugal; MNE/IFA, Romania; MES of Russia and NRC KI, Russian Federation; JINR; MESTD, Serbia; MSSR, Slovakia; ARRS and MIZŠ, Slovenia; DST/NRF, South Africa; MINECO, Spain; SRC and Wallenberg Foundation, Sweden; SERI, SNSF and Cantons of Bern and Geneva, Switzerland; MOST, Taiwan; TAEK, Turkey; STFC, United Kingdom; DOE and NSF, United States of America. In addition, individual groups and members have received support from BCKDF, the Canada Council, CANARIE, CRC, Compute Canada, FQRNT, and the Ontario Innovation Trust, Canada; EPLANET, ERC, FP7, Horizon 2020 and Marie Skłodowska-Curie Actions, European Union; Investissements d'Avenir Labex and Idex, ANR, Region Auvergne and Fondation Partager le Savoir, France; DFG and AvH Foundation, Germany; Herakleitos, Thales and Aristeia programmes co-financed by EU-ESF and the Greek NSRF; BSF, GIF and Minerva, Israel; BRF, Norway; the Royal Society and Leverhulme Trust, United Kingdom.

The crucial computing support from all WLCG partners is acknowledged gratefully, in particular from CERN and the ATLAS Tier-1 facilities at TRIUMF (Canada), NDGF (Denmark, Norway, Sweden), CC-IN2P3 (France), KIT/GridKA (Germany), INFN-CNAF (Italy), NL-T1 (Netherlands), PIC (Spain), ASGC (Taiwan), RAL (UK) and BNL (USA) and in the Tier-2 facilities worldwide.

References

[1] Yu. A. Golfand and E. P. Likhtman,
Extension of the Algebra of Poincare Group Generators and Violation of P Invariance,
JETP Lett. **13** (1971) 323, [Pisma Zh. Eksp. Teor. Fiz.13,452(1971)].

[2] D. V. Volkov and V. P. Akulov, *Is the Neutrino a Goldstone Particle?*, Phys. Lett. **B46** (1973) 109.

[3] J. Wess and B. Zumino, *Supergauge Transformations in Four-Dimensions*,
Nucl. Phys. **B70** (1974) 39.

[4] J. Wess and B. Zumino, *Supergauge Invariant Extension of Quantum Electrodynamics*,
Nucl. Phys. **B78** (1974) 1.

[5] S. Ferrara and B. Zumino, *Supergauge Invariant Yang-Mills Theories*,
Nucl. Phys. **B79** (1974) 413.

[6] A. Salam and J. A. Strathdee, *Supersymmetry and Nonabelian Gauges*,
Phys. Lett. **B51** (1974) 353.

[7] S. P. Martin, *A Supersymmetry primer* (1997), [Adv. Ser. Direct. High Energy Phys.18,1(1998)],
arXiv: hep-ph/9709356.

[8] P. Fayet, *Supersymmetry and Weak, Electromagnetic and Strong Interactions*,
Phys. Lett. **B64** (1976) 159.

[9] P. Fayet, *Spontaneously Broken Supersymmetric Theories of Weak, Electromagnetic and Strong Interactions*, Phys. Lett. **B69** (1977) 489.

[10] G. R. Farrar and P. Fayet, *Phenomenology of the Production, Decay, and Detection of New Hadronic States Associated with Supersymmetry*, Phys. Lett. **B76** (1978) 575.

[11] H. Goldberg, *Constraint on the Photino Mass from Cosmology*,
Phys. Rev. Lett. **50** (1983) 1419, [Erratum: Phys. Rev. Lett. **103** (2009) 099905].

[12] J. R. Ellis et al., *Supersymmetric Relics from the Big Bang*, Nucl. Phys. **B238** (1984) 453.

[13] N. Sakai, *Naturalness in Supersymmetric Guts*, Z. Phys. **C11** (1981) 153.

[14] S. Dimopoulos, S. Raby and F. Wilczek, *Supersymmetry and the Scale of Unification*,
Phys. Rev. **D24** (1981) 1681.

[15] L. E. Ibanez and G. G. Ross, *Low-Energy Predictions in Supersymmetric Grand Unified Theories*,
Phys. Lett. **B105** (1981) 439.

[16] S. Dimopoulos and H. Georgi, *Softly Broken Supersymmetry and SU(5)*,
Nucl. Phys. **B193** (1981) 150.

[17] R. Barbieri and G. F. Giudice, *Upper Bounds on Supersymmetric Particle Masses*,
Nucl. Phys. **B306** (1988) 63.

[18] B. de Carlos and J. A. Casas, *One loop analysis of the electroweak breaking in supersymmetric models and the fine tuning problem*, Phys. Lett. **B309** (1993) 320, arXiv: hep-ph/9303291.

[19] K. Inoue et al., *Aspects of Grand Unified Models with Softly Broken Supersymmetry*, Prog. Theor. Phys. **68** (1982) 927, [Erratum: Prog. Theor. Phys. **70** (1983) 330].

[20] J. R. Ellis and S. Rudaz, *Search for Supersymmetry in Toponium Decays*, Phys. Lett. **B128** (1983) 248.

[21] C. Borschensky et al., *Squark and gluino production cross sections in pp collisions at $\sqrt{s}$ = 13, 14, 33 and 100 TeV*, Eur.Phys.J. **C74** (2014) 3174, arXiv: 1407.5066 [hep-ph].

[22] ATLAS Collaboration, *Search for supersymmetry at $\sqrt{s}$=8 TeV in final states with jets and two same-sign leptons or three leptons with the ATLAS detector*, JHEP **06** (2014) 035, arXiv: 1404.2500 [hep-ex].

[23] ATLAS Collaboration, *The ATLAS Experiment at the CERN Large Hadron Collider*, JINST **3** (2008) S08003.

[24] CMS Collaboration, *Search for new physics in events with same-sign dileptons and jets in pp collisions at $\sqrt{s}$ = 8 TeV*, JHEP **01** (2014) 163, [Erratum: JHEP **01** (2015) 014], arXiv: 1311.6736 [hep-ph].

[25] ATLAS Collaboration, *ATLAS Insertable B-Layer Technical Design Report*, CERN-LHCC-2010-013. ATLAS-TDR-19, 2010, URL: http://cds.cern.ch/record/1291633.

[26] ATLAS Collaboration, *Improved luminosity determination in pp collisions at $\sqrt{s}$ = 7 TeV using the ATLAS detector at the LHC*, Eur. Phys. J. C **73** (2013) 2518, arXiv: 1302.4393 [hep-ex].

[27] ATLAS Collaboration, *The ATLAS Simulation Infrastructure*, Eur.Phys.J. **C70** (2010) 823, arXiv: 1005.4568 [physics.ins-det].

[28] S. Agostinelli et al., *GEANT4: A Simulation toolkit*, Nucl.Instrum.Meth. **A506** (2003) 250.

[29] ATLAS Collaboration, *The simulation principle and performance of the ATLAS fast calorimeter simulation FastCaloSim*, ATL-PHYS-PUB-2010-013, 2010, URL: http://cds.cern.ch/record/1300517.

[30] T. Gleisberg et al., *Event generation with SHERPA 1.1*, JHEP **02** (2009) 007, arXiv: 0811.4622 [hep-ph].

[31] ATLAS Collaboration, *Multi-Boson Simulation for 13 TeV ATLAS Analyses*, ATL-PHYS-PUB-2016-002, 2016, URL: http://cds.cern.ch/record/2119986.

[32] T. Gleisberg and S. Höche, *Comix, a new matrix element generator*, JHEP **12** (2008) 039, arXiv: 0808.3674 [hep-ph].

[33] F. Cascioli, P. Maierhofer and S. Pozzorini, *Scattering Amplitudes with Open Loops*, Phys. Rev. Lett. **108** (2012) 111601, arXiv: 1111.5206 [hep-ph].

[34] S. Schumann and F. Krauss, *A Parton shower algorithm based on Catani-Seymour dipole factorisation*, JHEP **03** (2008) 038, arXiv: 0709.1027 [hep-ph].

[35] S. Höche et al., *QCD matrix elements + parton showers: The NLO case*, JHEP **04** (2013) 027, arXiv: 1207.5030 [hep-ph].

[36] H.-L. Lai et al., *New parton distributions for collider physics*, Phys.Rev. **D82** (2010) 074024, arXiv: 1007.2241 [hep-ph].

[37] J. Alwall et al., *MadGraph 5 : Going Beyond*, JHEP **06** (2011) 128, arXiv: 1106.0522 [hep-ph].

[38] T. Sjöstrand, S. Mrenna and P. Z. Skands, *A Brief Introduction to PYTHIA 8.1*, Comput. Phys. Commun. **178** (2008) 852, arXiv: 0710.3820 [hep-ph].

[39] ATLAS Collaboration, *Modelling of the $t\bar{t}H$ and $t\bar{t}V$ ($V = W, Z$) processes for $\sqrt{s} = 13$ TeV ATLAS analyses*, ATL-PHYS-PUB-2015-022, 2016, URL: http://cds.cern.ch/record/2120826.

[40] ATLAS Collaboration, *ATLAS Pythia8 tunes to 7 TeV data*, ATL-PHYS-PUB-2014-021, 2014, URL: http://cds.cern.ch/record/1966419.

[41] R. D. Ball et al., *Parton distributions with LHC data*, Nucl. Phys. **B867** (2013) 244, arXiv: 1207.1303 [hep-ph].

[42] J. Alwall et al., *The automated computation of tree-level and next-to-leading order differential cross sections, and their matching to parton shower simulations*, JHEP **07** (2014) 079, arXiv: 1405.0301 [hep-ph].

[43] G. Corcella et al., *HERWIG 6: An Event generator for hadron emission reactions with interfering gluons (including supersymmetric processes)*, JHEP **01** (2001) 010, arXiv: hep-ph/0011363.

[44] J. Pumplin et al., *New generation of parton distributions with uncertainties from global QCD analysis*, JHEP **07** (2002) 012, arXiv: hep-ph/0201195.

[45] LHC Higgs Cross Section Working Group, *Handbook of LHC Higgs Cross Sections: 2. Differential Distributions*, CERN-2012-002 (CERN, Geneva, 2012), arXiv: 1201.3084 [hep-ph].

[46] L. Lönnblad and S. Prestel, *Matching Tree-Level Matrix Elements with Interleaved Showers*, JHEP **03** (2012) 019, arXiv: 1109.4829 [hep-ph].

[47] W. Beenakker et al., *Squark and gluino production at hadron colliders*, Nucl.Phys. **B492** (1997) 51, arXiv: hep-ph/9610490.

[48] A. Kulesza and L. Motyka, *Threshold resummation for squark-antisquark and gluino-pair production at the LHC*, Phys.Rev.Lett. **102** (2009) 111802, arXiv: 0807.2405 [hep-ph].

[49] A. Kulesza and L. Motyka, *Soft gluon resummation for the production of gluino-gluino and squark-antisquark pairs at the LHC*, Phys.Rev. **D80** (2009) 095004, arXiv: 0905.4749 [hep-ph].

[50] W. Beenakker et al., *Soft-gluon resummation for squark and gluino hadroproduction*, JHEP **12** (2009) 041, arXiv: 0909.4418 [hep-ph].

[51] W. Beenakker et al., *Squark and gluino hadroproduction*, Int.J.Mod.Phys. **A26** (2011) 2637, arXiv: 1105.1110 [hep-ph].

[52] M. Krämer et al., *Supersymmetry production cross sections in pp collisions at $\sqrt{s} = 7$ TeV* (2012), arXiv: 1206.2892 [hep-ph].

[53] D. J. Lange, *The EvtGen particle decay simulation package*, Nucl. Instrum. Meth. **A462** (2001) 152.

[54] ATLAS Collaboration, *Summary of ATLAS Pythia 8 tunes*, ATLAS-PHYS-PUB-2012-003, 2012, URL: http://cdsweb.cern.ch/record/1474107.

[55] A. D. Martin et al., *Parton distributions for the LHC*, Eur. Phys. J. **C63** (2009) 189, arXiv: 0901.0002 [hep-ph].

[56] ATLAS Collaboration, *Vertex Reconstruction Performance of the ATLAS Detector at* $\sqrt{s}$ = 13 *TeV*, ATL-PHYS-PUB-2015-026, 2015, URL: http://cdsweb.cern.ch/record/2037717.

[57] ATLAS Collaboration, *Electron efficiency measurements with the ATLAS detector using the 2012 LHC proton-proton collision data*, ATLAS-CONF-2014-032, 2014, URL: http://cds.cern.ch/record/1706245.

[58] ATLAS Collaboration, *Electron identification measurements in ATLAS using* $\sqrt{s}$ = *13 TeV data with 50 ns bunch spacing*, ATL-PHYS-PUB-2015-041, 2015, URL: http://cds.cern.ch/record/2048202.

[59] ATLAS Collaboration, *Muon reconstruction performance in early Run II*, ATL-PHYS-PUB-2015-037, 2015, URL: http://cds.cern.ch/record/2047831.

[60] M. Cacciari, G. P. Salam and G. Soyez, *The anti-kt jet clustering algorithm*, JHEP **04** (2008) 063, arXiv: 0802.1189 [hep-ph].

[61] W. Lampl et al., *Calorimeter Clustering Algorithms: Description and Performance*, ATL-LARG-PUB-2008-002, 2008, URL: http://cdsweb.cern.ch/record/1099735.

[62] ATLAS Collaboration, *Jet Calibration and Systematic Uncertainties for Jets Reconstructed in the ATLAS Detector at* $\sqrt{s}$ = 13 *TeV*, ATL-PHYS-PUB-2015-015, 2015, URL: http://cds.cern.ch/record/2028594.

[63] ATLAS Collaboration, *Tagging and suppression of pileup jets with the ATLAS detector*, ATLAS-CONF-2014-018, 2014, URL: http://cdsweb.cern.ch/record/1700870.

[64] ATLAS Collaboration, *Performance of b-Jet Identification in the ATLAS Experiment* (2015), arXiv: 1512.01094 [hep-ex].

[65] ATLAS Collaboration, *Expected performance of the ATLAS b-tagging algorithms in Run-2*, ATL-PHYS-PUB-2015-022, 2015, URL: http://cds.cern.ch/record/2037697.

[66] ATLAS Collaboration, *Performance of missing transverse momentum reconstruction for the ATLAS detector in the first proton-proton collisions at at* $\sqrt{s}$= *13 TeV*, ATL-PHYS-PUB-2015-027, 2015, URL: http://cds.cern.ch/record/2037904.

[67] ATLAS Collaboration, *Expected performance of missing transverse momentum reconstruction for the ATLAS detector at* $\sqrt{s}$ = *13 TeV*, ATL-PHYS-PUB-2015-023, 2015, URL: http://cds.cern.ch/record/2037700.

[68] T. Sjöstrand, S. Mrenna and P. Z. Skands, *PYTHIA 6.4 Physics and Manual*, JHEP **05** (2006) 026, arXiv: hep-ph/0603175.

[69] M. Baak et al., *HistFitter software framework for statistical data analysis*, Eur. Phys. J. **C75** (2015) 153, arXiv: 1410.1280 [hep-ex].

[70] G. Cowan et al., *Asymptotic formulae for likelihood-based tests of new physics*, Eur. Phys. J. **C71** (2011) 1554, [Erratum: Eur. Phys. J. **C73** (2013) 2501], arXiv: 1007.1727 [physics.data-an].

[71] A. L. Read, *Presentation of search results: the CL s technique*, Journal of Physics G: Nuclear and Particle Physics **28** (2002) 2693.

[72] ATLAS Collaboration, *Summary of the searches for squarks and gluinos using $\sqrt{s} = 8$ TeV pp collisions with the ATLAS experiment at the LHC*, JHEP **10** (2015) 054, arXiv: 1507.05525 [hep-ex].

[73] ATLAS Collaboration, *ATLAS Run 1 searches for direct pair production of third-generation squarks at the Large Hadron Collider*, Eur. Phys. J. **C75** (2015) 510, arXiv: 1506.08616 [hep-ex].

[74] ATLAS Collaboration, *Search for direct top-squark pair production in final states with two leptons in pp collisions at $\sqrt{s} = 8$ TeV with the ATLAS detector*, JHEP **06** (2014) 124, arXiv: 1403.4853v1 [hep-ex].

Auxiliary material

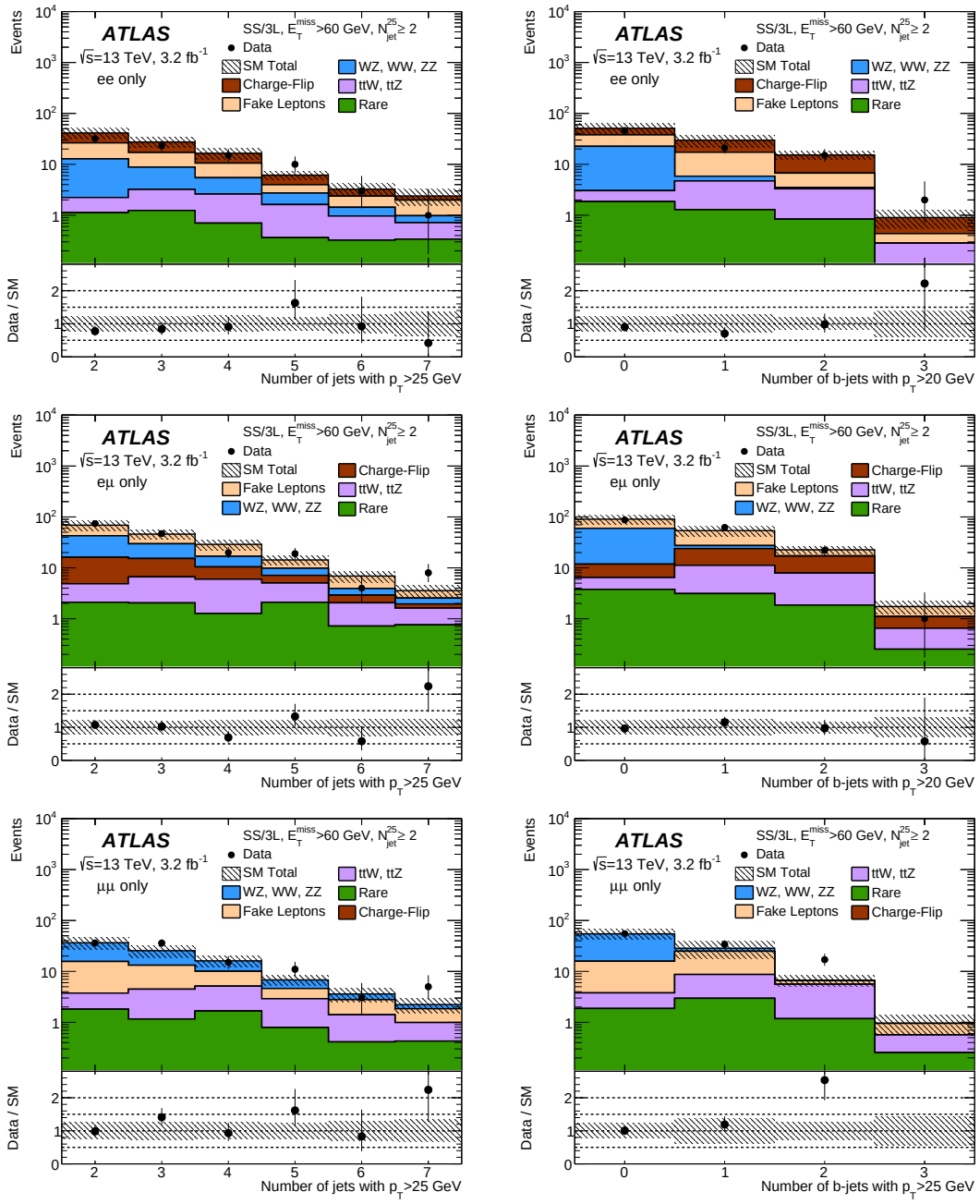

Figure 1: Distributions of the number of jets with $p_{\mathrm{T}} > 25$ GeV (left) and number of b-jets with $p_{\mathrm{T}} > 20$ GeV (right) for events in the ee (top), $e\mu$ (middle) and $\mu\mu$ channels (bottom). The statistical uncertainties in the background prediction are included in the uncertainty band, as well as the theory uncertainties for the backgrounds with prompt SS/3L, and the full systematic uncertainties for data-driven backgrounds. The last bin includes overflows. The "Fake leptons" category corresponds to FNP leptons (see text), and the "Rare" category contains the contributions from associated production of $t\bar{t}$ with $h/WW/t/t\bar{t}$, as well as tZ, Wh, Zh, and triboson production. The lower part of the figure shows the ratio of data to the background prediction.

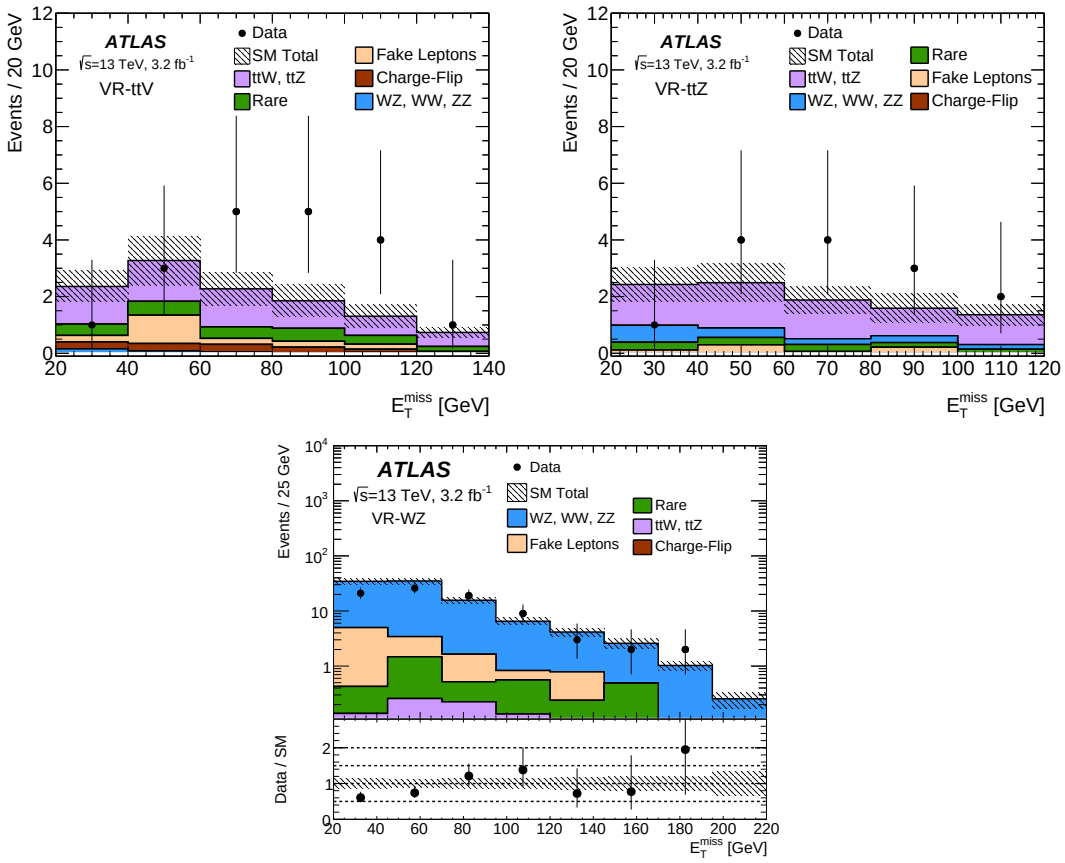

Figure 2: Missing transverse momentum distribution in VR-ttV (top left), VR-ttZ (top right) and VR-WZ (bottom). The statistical uncertainties in the background prediction are included in the uncertainty band, as well as the theory uncertainties for the backgrounds with prompt SS/3L, and the full systematic uncertainties for data-driven backgrounds. The last bin includes overflows. The "Fake leptons" category corresponds to FNP leptons (see text), and the "Rare" category contains the contributions from associated production of $t\bar{t}$ with $h/WW/t/t\bar{t}$, as well as tZ, Wh, Zh, and triboson production. When shown, the lower part of the figure shows the ratio of data to the background prediction.

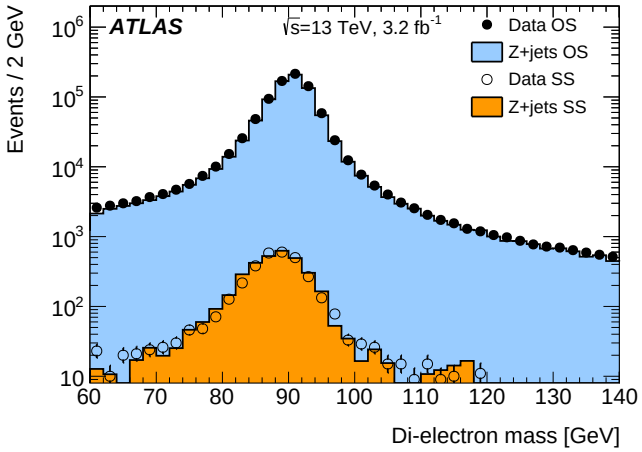

Figure 3: Distributions of the invariant mass for opposite-sign (OS) and same-sign (SS) dielectron pairs. Data are shown with full (open) circles for OS (SS) dielectron pairs including statistical uncertainty, and are compared with the expected contribution from simulated $Z \rightarrow ee$ events (filled areas).

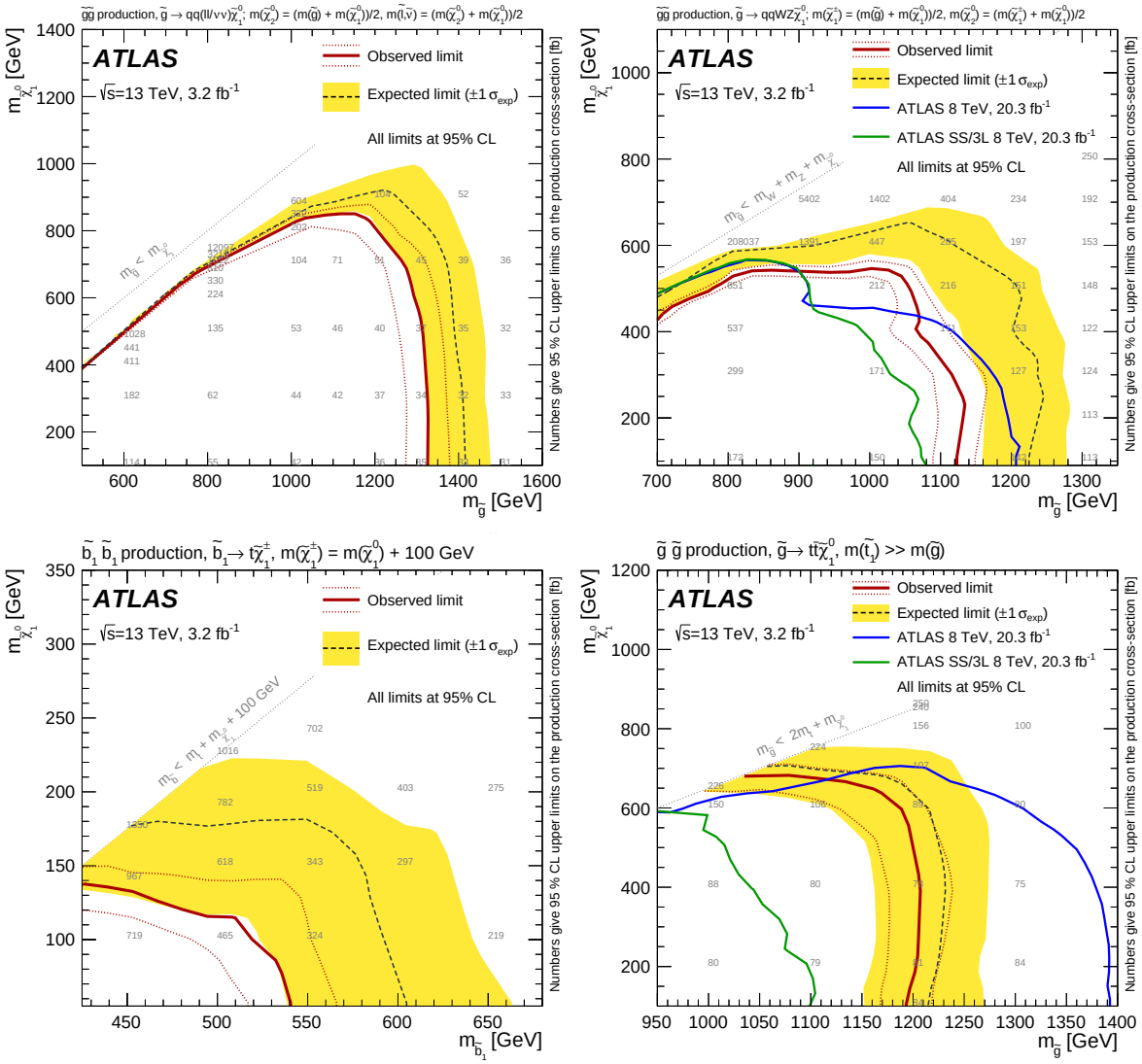

Figure 4: Observed and expected exclusion limits on the $\tilde{g}$, $\tilde{b}_1$and $\tilde{\chi}_1^0$ masses in the context of SUSY scenarios with simplified mass spectra featuring $\tilde{g}\tilde{g}$ or $\tilde{b}_1\tilde{b}_1^*$ pair production with exclusive decay modes. The contours of the band around the expected limit are the $\pm 1\sigma$ results, including all uncertainties except theoretical uncertainties on the signal cross-section. The dotted lines around the observed limit illustrate the change in the observed limit as the nominal signal cross-section is scaled up and down by the theoretical uncertainty. All limits are computed at 95% CL. Results are compared with the limits obtained by previous ATLAS searches [22, 72, 73]. The grey numbers show 95% CL upper limits on cross-sections (in fb) obtained using the signal efficiency and acceptance specific to each model.

Table 1: Comparison of the predicted number of background events in the validation regions using the nominal estimates obtained from data and the cross-check estimates based on MC with corrections derived in dedicated control regions. Both the statistical and systematic uncertainties are shown in the table.

		VR-WW	VR-WZ	VR-ttV	VR-ttZ
Fake/non-prompt	Nominal	0.6 ± 0.5	8 ± 6	2.1 ± 1.4	0.6 ± 1.0
	MC based	0.01 ± 0.01	3.4 ± 1.8	1.8 ± 1.0	0.5 ± 0.4
Charge-flip	Nominal	0.26 ± 0.05	–	1.14 ± 0.15	–
	MC based	< 0.08	–	0.27 ± 0.23	–

Table 2: Comparison of the predicted number of background events in the signal regions using the nominal estimates obtained from data and the cross-check estimates based on MC with corrections derived in dedicated control regions. Both the statistical and systematic uncertainties are shown in the table.

		SR0b3j	SR0b5j	SR1b	SR3b
Fake/non-prompt leptons	Nominal	< 0.2	0.05 ± 0.18	0.8 ± 0.8	0.13 ± 0.17
	MC based	< 0.15	< 0.15	2.7 ± 1.9	0.02 ± 0.01
Charge-flip	Nominal	–	0.02 ± 0.01	0.60 ± 0.12	0.19 ± 0.06
	MC based	–	< 0.08	1.0 ± 0.8	< 0.08

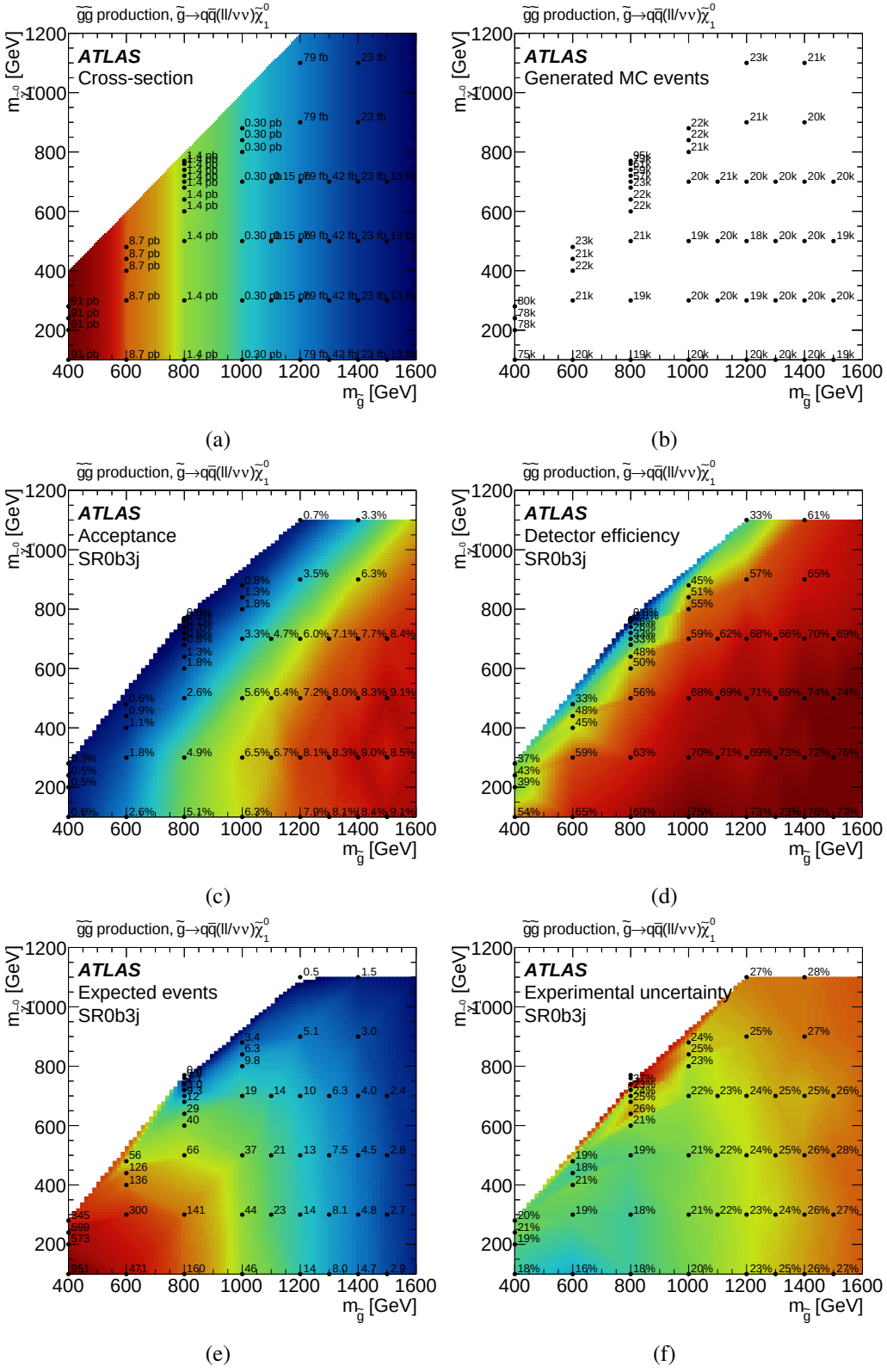

Figure 5: SUSY scenario with $\tilde{g}\tilde{g}$ production and $\tilde{g} \rightarrow q\bar{q}\ell\ell\tilde{\chi}_1^0$ decay: (a) production cross-section, (b) number of generated MC events, (c) signal acceptance and (d) reconstruction efficiency in the signal region SR0b3j, (e) corresponding expected signal yield and (f) associated uncertainty due to experimental sources. The benchmark scenarios used to set exclusion limits are materialized by black dot markers. Acceptance and efficiency are defined as in appendix A of [74].

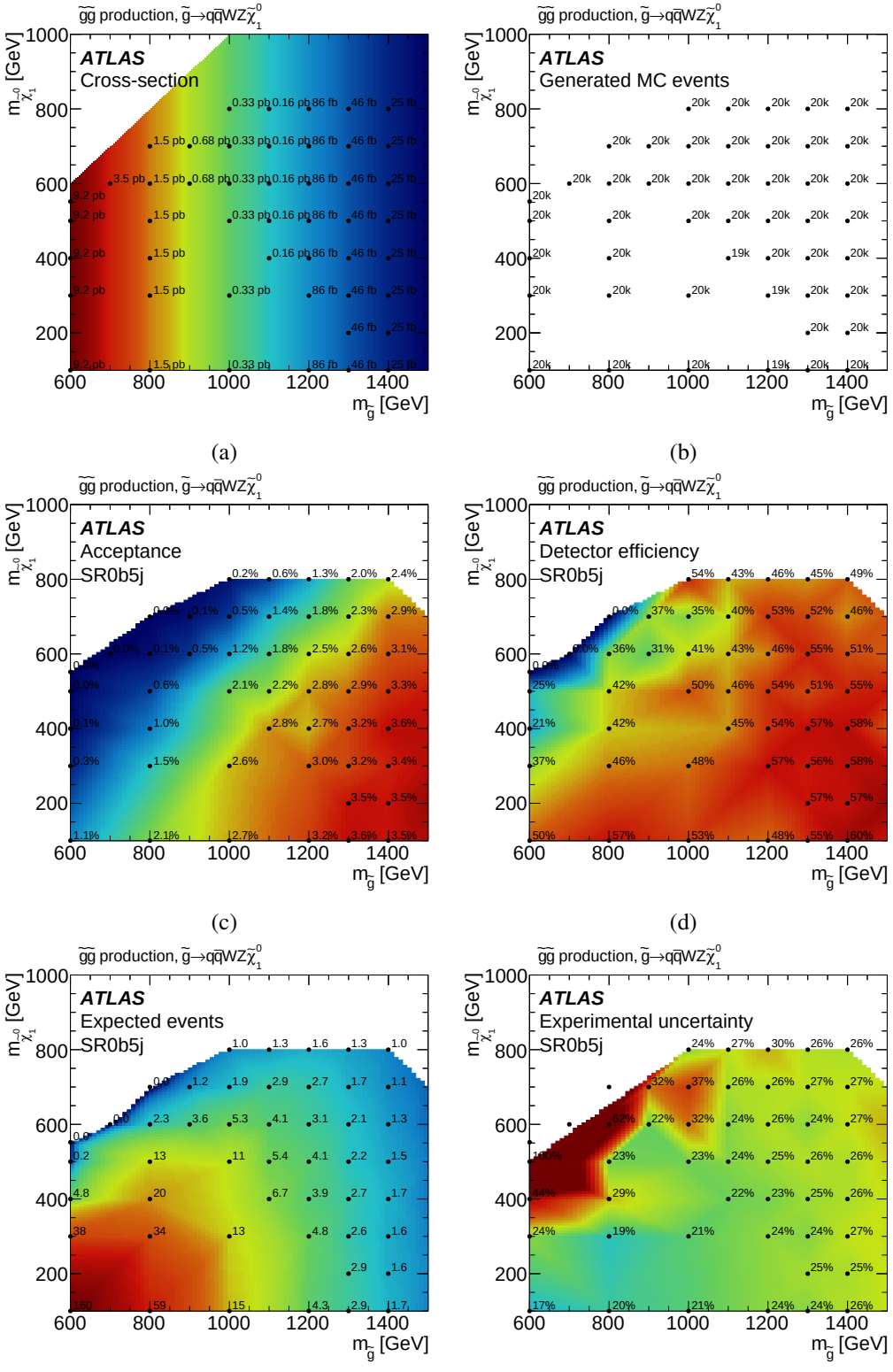

Figure 6: SUSY scenario with $\tilde{g}\tilde{g}$ production and $\tilde{g} \rightarrow q\bar{q}WZ\tilde{\chi}_1^0$ decay: (a) production cross-section, (b) number of generated MC events, (c) signal acceptance and (d) reconstruction efficiency in the signal region SR0b5j, (e) corresponding expected signal yield and (f) associated uncertainty due to experimental sources. The benchmark scenarios used to set exclusion limits are materialized by black dot markers. Acceptance and efficiency are defined as in appendix A of [74].

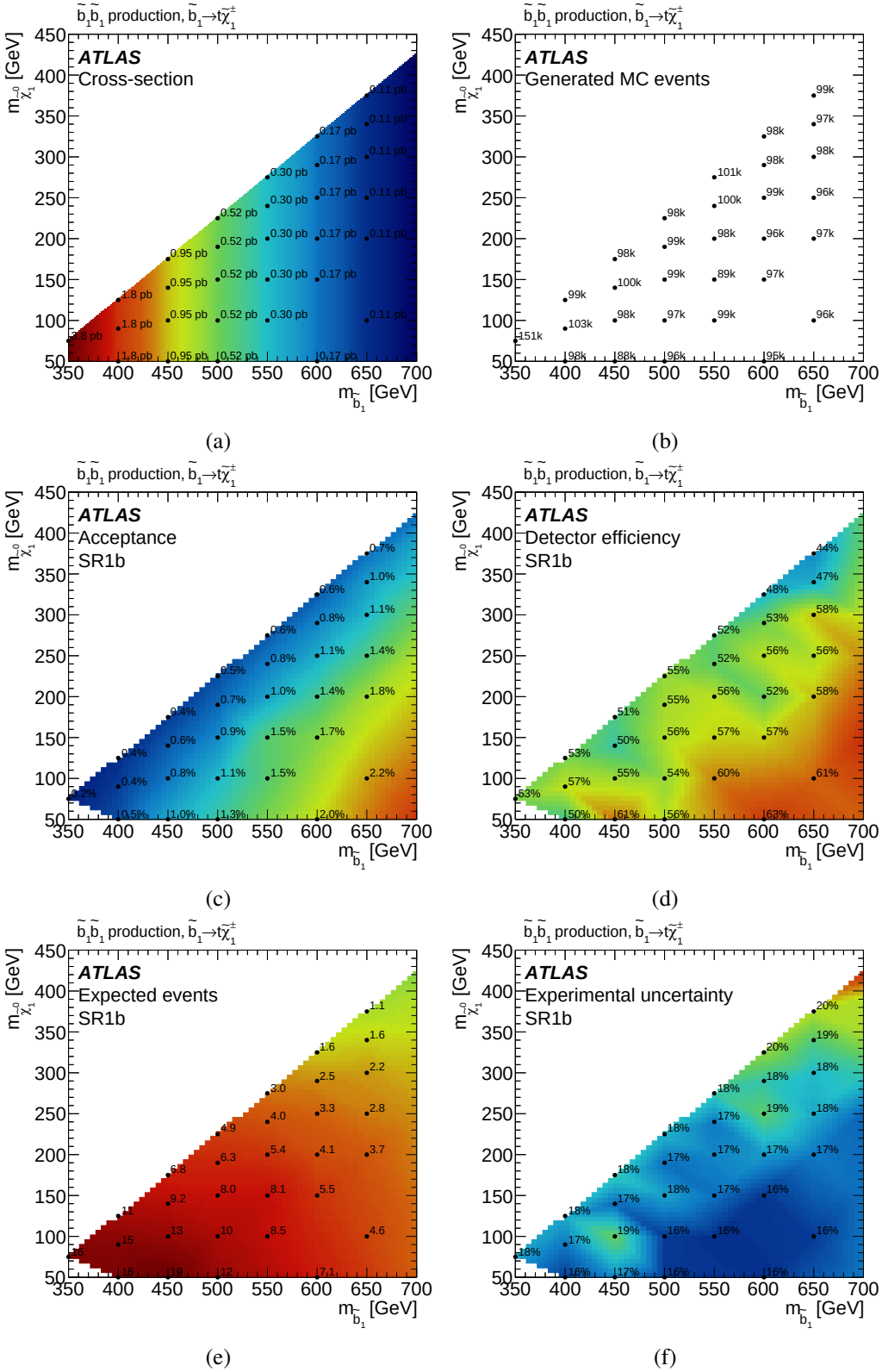

Figure 7: SUSY scenario with $\tilde{b}_1\tilde{b}_1$ production and $\tilde{b}_1 \to tW\tilde{\chi}_1^0$ decay: (a) production cross-section, (b) number of generated MC events, (c) signal acceptance and (d) reconstruction efficiency in the signal region SR1b, (e) corresponding expected signal yield and (f) associated uncertainty due to experimental sources. The benchmark scenarios used to set exclusion limits are materialized by black dot markers. Acceptance and efficiency are defined as in appendix A of [74].

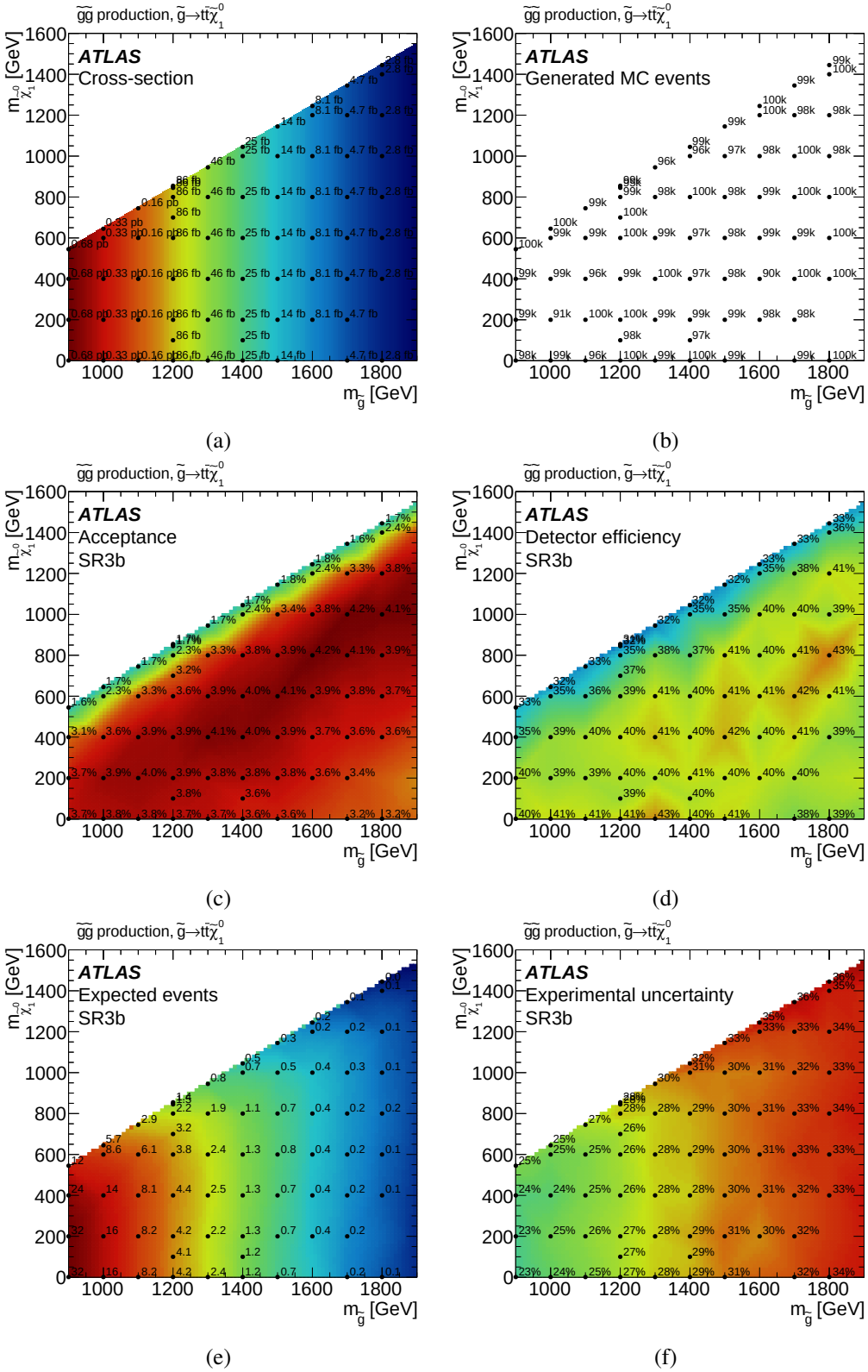

Figure 8: SUSY scenario with $\tilde{g}\tilde{g}$ production and $\tilde{g} \rightarrow t\bar{t}\tilde{\chi}_1^0$ decay: (a) production cross-section, (b) number of generated MC events, (c) signal acceptance and (d) reconstruction efficiency in the signal region SR3b, (e) corresponding expected signal yield and (f) associated uncertainty due to experimental sources. The benchmark scenarios used to set exclusion limits are materialized by black dot markers. Acceptance and efficiency are defined as in appendix A of [74].

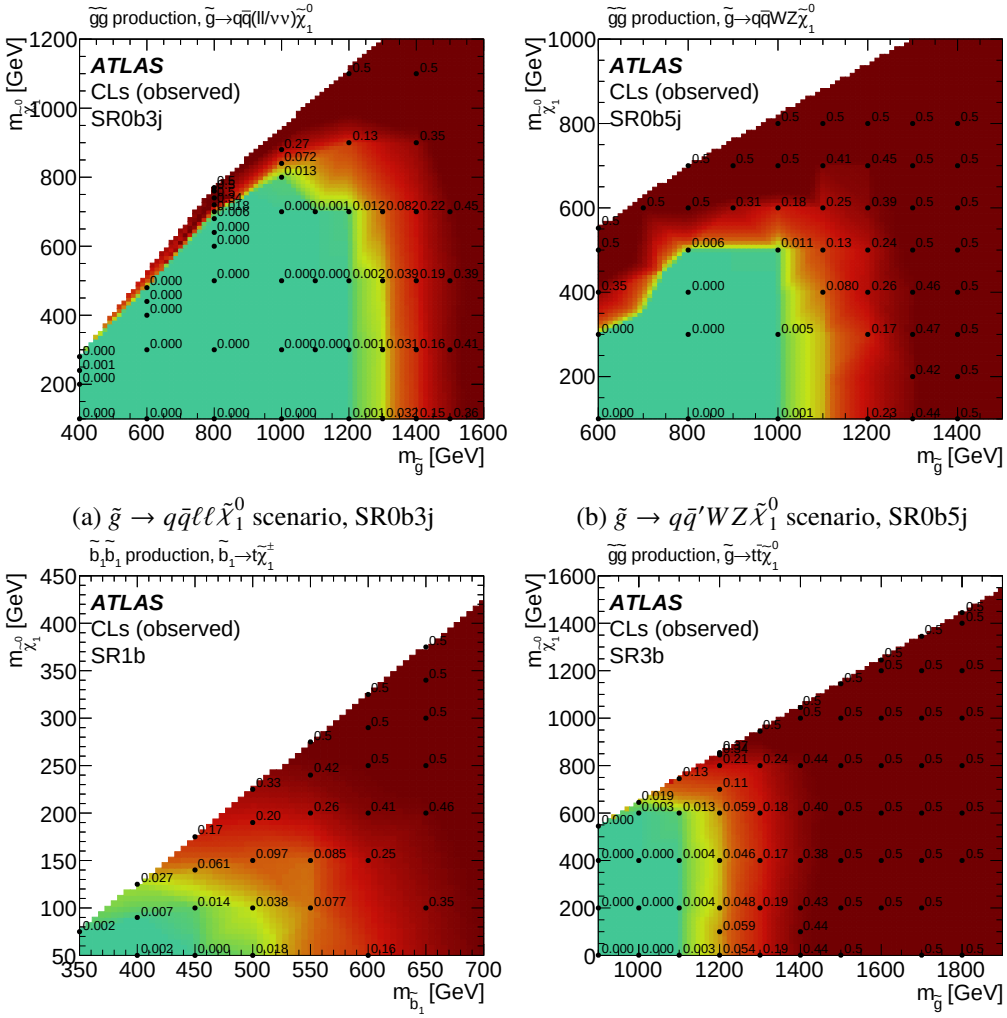

(a) $\tilde{g} \to q\bar{q}\ell\ell\tilde{\chi}_1^0$ scenario, SR0b3j

(b) $\tilde{g} \to q\bar{q}'WZ\tilde{\chi}_1^0$ scenario, SR0b5j

(c) $\tilde{b}_1 \to tW^-\tilde{\chi}_1^0$ scenario, SR1b

(d) $\tilde{g} \to t\bar{t}\tilde{\chi}_1^0$ scenario, SR3b

Figure 9: Observed CL_s in the four signal regions. The benchmark scenarios used to set exclusion limits are materialized by black dot markers.

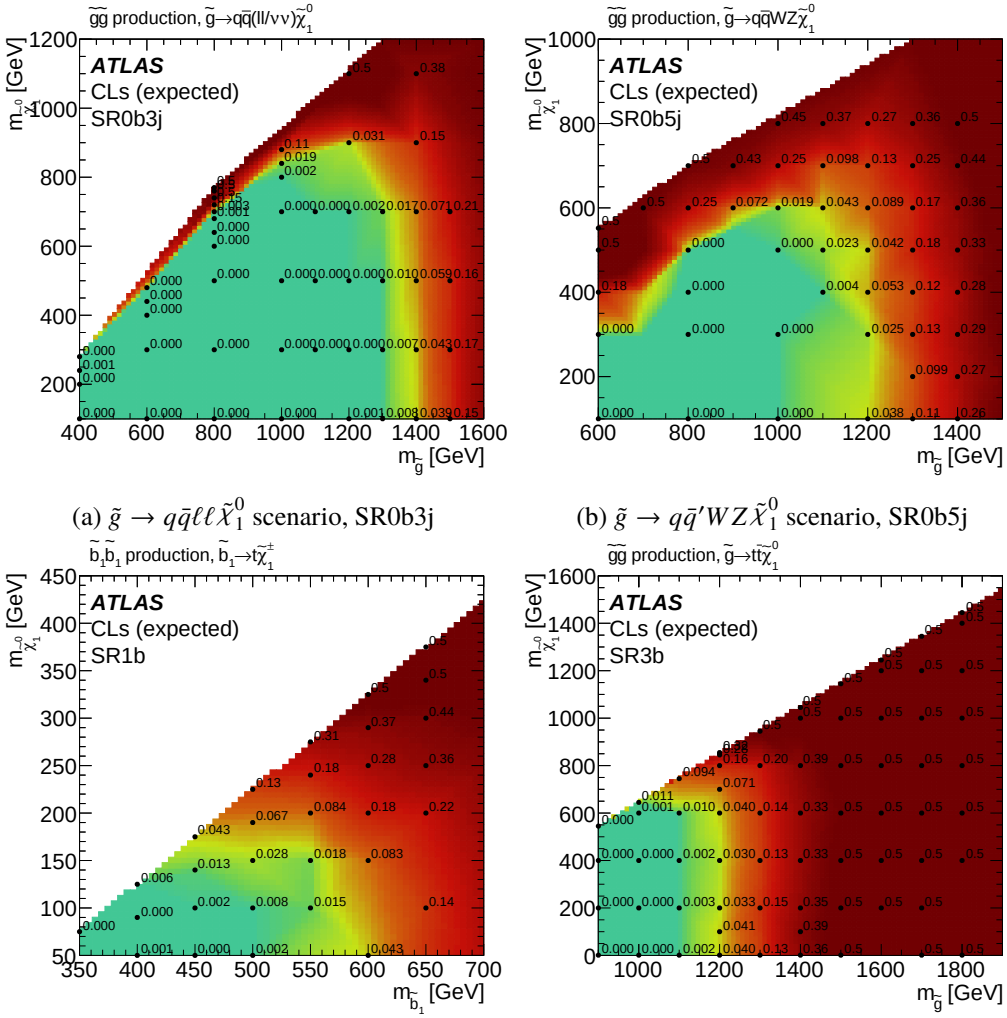

(a) $\tilde{g} \to q\bar{q}\ell\ell\tilde{\chi}_1^0$ scenario, SR0b3j

(b) $\tilde{g} \to q\bar{q}'WZ\tilde{\chi}_1^0$ scenario, SR0b5j

(c) $\tilde{b}_1 \to tW^-\tilde{\chi}_1^0$ scenario, SR1b

(d) $\tilde{g} \to t\bar{t}\tilde{\chi}_1^0$ scenario, SR3b

Figure 10: Expected CL_s in the four signal regions. The benchmark scenarios used to set exclusion limits are materialized by black dot markers.

Table 3: Number of signal events selected at different stages of the signal regions definitions, for the four benchmark scenarios shown on Fig. 3. Only the statistical uncertainties are displayed.

	Raw events	Number of events expected for $L = 3.2$ fb^{-1}
SR0b3j, $\tilde{g} \to q\bar{q}(\ell\ell/\nu\nu)\tilde{\chi}_1^0$, $m_{\tilde{g}} = 1.3$ TeV, $m_{\tilde{\chi}_1^0} = 500$ GeV		
produced	20051	148
≥ 3 leptons ($p_{\mathrm{T}} > 20, 20, 10$ GeV)	2026	14.4 ± 0.4
trigger	2024	14.3 ± 0.4
no b-jet ($p_{\mathrm{T}} > 20$ GeV)	1665	11.66 ± 0.33
≥ 3 jets ($p_{\mathrm{T}} > 50$ GeV)	1556	10.91 ± 0.32
$E_{\mathrm{T}}^{\mathrm{miss}} > 200$ GeV	1079	7.52 ± 0.27
$m_{\mathrm{eff}} > 550$ GeV	1079	7.52 ± 0.27
SR0b5j, $\tilde{g} \to q\bar{q}WZ\tilde{\chi}_1^0$, $m_{\tilde{g}} = 1.1$ TeV, $m_{\tilde{\chi}_1^0} = 400$ GeV		
produced	19000	524
≥ 2 SS leptons ($p_{\mathrm{T}} > 20$ GeV)	646	18.7 ± 0.9
trigger	631	17.8 ± 0.9
no b-jet ($p_{\mathrm{T}} > 20$ GeV)	419	11.4 ± 0.7
≥ 5 jets ($p_{\mathrm{T}} > 50$ GeV)	300	8.1 ± 0.5
$E_{\mathrm{T}}^{\mathrm{miss}} > 125$ GeV	252	6.7 ± 0.5
$m_{\mathrm{eff}} > 650$ GeV	252	6.7 ± 0.5
SR1b, $\tilde{b}_1 \to t\tilde{\chi}_1^{\pm}$, $m_{\tilde{b}_1} = 600$ GeV, $m_{\tilde{\chi}_1^{\pm}} = 150$ GeV, $m_{\tilde{\chi}_1^0} = 50$ GeV		
produced	94706	560
≥ 2 SS leptons ($p_{\mathrm{T}} > 20$ GeV)	4115	25.5 ± 0.5
trigger	3901	23.1 ± 0.4
≥ 1 b-jet ($p_{\mathrm{T}} > 20$ GeV)	3367	20.0 ± 0.4
≥ 4 jets ($p_{\mathrm{T}} > 50$ GeV)	1881	11.23 ± 0.30
$E_{\mathrm{T}}^{\mathrm{miss}} > 150$ GeV	1148	7.08 ± 0.24
$m_{\mathrm{eff}} > 550$ GeV	1148	7.08 ± 0.24
SR3b, $\tilde{g} \to t\bar{t}\tilde{\chi}_1^0$, $m_{\tilde{g}} = 1.2$ TeV, $m_{\tilde{\chi}_1^0} = 700$ GeV		
produced	100000	275
≥ 2 SS leptons ($p_{\mathrm{T}} > 20$ GeV)	3535	9.28 ± 0.18
trigger	3386	8.53 ± 0.17
≥ 3 b-jets ($p_{\mathrm{T}} > 20$ GeV)	1704	4.26 ± 0.12
$E_{\mathrm{T}}^{\mathrm{miss}} > 125$ GeV	1320	3.31 ± 0.11
$m_{\mathrm{eff}} > 650$ GeV	1280	3.20 ± 0.10